

The kaobook class

**Use this document as a template**

# **Millikelvin Confocal Microscopy of Semiconductor Membranes and Filter Functions for Unital Quantum Operations**

**Customise this page according to your needs**

Tobias Hangleiter\*

September 7, 2025

\* A  $\text{\LaTeX}$  lover/hater

The harmony of the world is made manifest in Form and Number, and the heart and soul and all the poetry of Natural Philosophy are embodied in the concept of mathematical beauty.

– D'Arcy Wentworth Thompson

# Summary

# **Zusammenfassung**

# Acknowledgements

*Tobias Hangleiter  
Aachen, September 2025*

# Preface

It's been a journey.

*Tobias Hangleiter  
Aachen, September 2025*

## **How to read this thesis**

# Contents

<b>Summary</b>	<b>iii</b>
<b>Zusammenfassung</b>	<b>iv</b>
<b>Acknowledgements</b>	<b>v</b>
<b>Preface</b>	<b>vi</b>
<b>How to read this thesis</b>	<b>vii</b>
<b>Contents</b>	<b>viii</b>
<b>I A FLEXIBLE PYTHON TOOL FOR FOURIER-TRANSFORM NOISE SPECTROSCOPY</b>	<b>1</b>
<b>1 Introduction</b>	<b>2</b>
<b>2 Theory of spectral noise estimation</b>	<b>4</b>
2.1 Spectrum estimation from time series . . . . .	5
2.2 Window functions . . . . .	7
2.3 Welch’s method . . . . .	9
2.4 Parameters & Properties of the PSD . . . . .	9
<b>3 The python_spectrometer software package</b>	<b>11</b>
3.1 Package design and implementation . . . . .	11
3.1.1 Data acquisition . . . . .	11
3.1.2 Data processing . . . . .	13
3.2 Feature overview . . . . .	15
3.2.1 Serial spectrum acquisition . . . . .	15
3.2.2 Live spectrum acquisition . . . . .	19
<b>4 Conclusion and outlook</b>	<b>21</b>
<b>II CHARACTERIZATION AND IMPROVEMENTS OF A MILLIKELVIN CONFOCAL MICROSCOPE</b>	<b>24</b>
<b>III OPTICAL MEASUREMENTS OF ELECTROSTATIC EXCITON TRAPS IN SEMICONDUCTOR MEMBRANES</b>	<b>25</b>
<b>IV A FILTER-FUNCTION FORMALISM FOR UNITAL QUANTUM OPERATIONS</b>	<b>26</b>
<b>5 Introduction</b>	<b>27</b>
<b>6 Filter-function formalism for unital quantum operations</b>	<b>31</b>
6.1 Transfer matrix representation of quantum operations . . . . .	31
6.1.1 Brief review of quantum operations and superoperators . . . . .	31
6.1.2 Liouville representation of the error channel . . . . .	32
6.2 Calculating the decay amplitudes . . . . .	37
6.2.1 Control matrix of a gate sequence . . . . .	39
6.2.2 Control matrix of a single gate . . . . .	40



6.3	Calculating the frequency shifts . . . . .	41
6.4	Computing derived quantities . . . . .	43
6.4.1	Average gate and entanglement fidelity . . . . .	43
6.4.2	State fidelity and measurements . . . . .	44
6.4.3	Leakage . . . . .	45
6.5	Performance analysis and efficiency improvements . . . . .	45
6.6	Periodic Hamiltonians . . . . .	46
6.7	Extending Hilbert spaces . . . . .	46
6.8	Operator bases . . . . .	47
6.9	Computational complexity . . . . .	48
<b>7</b>	<b>Filter functions from random sampling</b>	<b>52</b>
7.1	Reconstruction by frequency-comb time domain simulation . . . . .	52
7.2	Case studies . . . . .	54
<b>8</b>	<b>The filter_functions software package</b>	<b>58</b>
8.1	Package overview . . . . .	58
8.2	Workflow . . . . .	59
<b>9</b>	<b>Example applications</b>	<b>62</b>
9.1	Singlet-triplet two-qubit gates . . . . .	62
9.2	Rabi driving . . . . .	64
9.3	Randomized Benchmarking . . . . .	67
9.4	Quantum Fourier transform . . . . .	70
<b>10</b>	<b>Conclusion and outlook</b>	<b>73</b>
	<b>APPENDIX</b>	<b>75</b>
<b>A</b>	<b>Supplementary to Part IV: Filter-function derivations and validation</b>	<b>76</b>
A.1	Additional derivations . . . . .	76
A.1.1	Derivation of the single-qubit cumulant function in the Liouville representation . .	76
A.1.2	Evaluation of the integrals in Equation 6.40 . . . . .	77
A.1.3	Simplifying the calculation of the entanglement infidelity . . . . .	78
A.1.4	Sum rule . . . . .	78
A.2	Convergence Bounds . . . . .	79
A.2.1	Magnus Expansion . . . . .	79
A.2.2	Infidelity . . . . .	81
A.3	Concatenation of second-order filter functions . . . . .	81
A.4	Monte Carlo and GKSL master equation simulations . . . . .	85
A.4.1	Simulation methods . . . . .	85
A.5	Fidelity validation . . . . .	87
A.5.1	Singlet-Triplet Gate Fidelity . . . . .	87
A.5.2	GRAPE-optimized gate set and validation of QFT fidelities . . . . .	88
	<b>Bibliography</b>	<b>91</b>
	<b>Glossary</b>	<b>94</b>
	<b>Figure source files and parameters</b>	<b>94</b>
	<b>Declaration of Authorship</b>	<b>96</b>

# Publications

- [1] Yaiza Aragonés-Soria, René Otten, Tobias Hangleiter, Pascal Cerfontaine, and David Gross. “Minimising Statistical Errors in Calibration of Quantum-Gate Sets.” June 7, 2022. doi: [10.48550/arXiv.2206.03417](https://doi.org/10.48550/arXiv.2206.03417). arXiv: [2206.03417](https://arxiv.org/abs/2206.03417) [quant-ph]. Pre-published.
- [2] Pascal Cerfontaine, Tobias Hangleiter, and Hendrik Bluhm. “Filter Functions for Quantum Processes under Correlated Noise.” In: *Physical Review Letters* 127.17 (Oct. 18, 2021), p. 170403. doi: [10.1103/PhysRevLett.127.170403](https://doi.org/10.1103/PhysRevLett.127.170403).
- [3] Thomas Descamps, Feng Liu, Sebastian Kindel, René Otten, Tobias Hangleiter, Chao Zhao, Mihail Ion Lepsa, Julian Ritzmann, Arne Ludwig, Andreas D. Wieck, Beata E. Kardynał, and Hendrik Bluhm. “Semiconductor Membranes for Electrostatic Exciton Trapping in Optically Addressable Quantum Transport Devices.” In: *Physical Review Applied* 19.4 (Apr. 28, 2023), p. 044095. doi: [10.1103/PhysRevApplied.19.044095](https://doi.org/10.1103/PhysRevApplied.19.044095).
- [4] Thomas Descamps, Feng Liu, Tobias Hangleiter, Sebastian Kindel, Beata E. Kardynał, and Hendrik Bluhm. “Millikelvin Confocal Microscope with Free-Space Access and High-Frequency Electrical Control.” In: *Review of Scientific Instruments* 95.8 (Aug. 9, 2024), p. 083706. doi: [10.1063/5.0200889](https://doi.org/10.1063/5.0200889).
- [5] Denny Dütz, Sebastian Kock, Tobias Hangleiter, and Hendrik Bluhm. “Distributed Bragg Reflectors for Thermal Isolation of Semiconductor Spin Qubits.” In preparation.
- [6] Sarah Fleitmann, Fabian Hader, Jan Vogelbruch, Simon Humpohl, Tobias Hangleiter, Stefanie Meyer, and Stefan van Waasen. “Noise Reduction Methods for Charge Stability Diagrams of Double Quantum Dots.” In: *IEEE Transactions on Quantum Engineering* 3 (2022), pp. 1–19. doi: [10.1109/TQE.2022.3165968](https://doi.org/10.1109/TQE.2022.3165968).
- [7] Fabian Hader, Jan Vogelbruch, Simon Humpohl, Tobias Hangleiter, Chimezie Eguzo, Stefan Heinen, Stefanie Meyer, and Stefan van Waasen. “On Noise-Sensitive Automatic Tuning of Gate-Defined Sensor Dots.” In: *IEEE Transactions on Quantum Engineering* 4 (2023), pp. 1–18. doi: [10.1109/TQE.2023.3255743](https://doi.org/10.1109/TQE.2023.3255743).
- [8] Tobias Hangleiter, Pascal Cerfontaine, and Hendrik Bluhm. “Filter-Function Formalism and Software Package to Compute Quantum Processes of Gate Sequences for Classical Non-Markovian Noise.” In: *Physical Review Research* 3.4 (Oct. 18, 2021), p. 043047. doi: [10.1103/PhysRevResearch.3.043047](https://doi.org/10.1103/PhysRevResearch.3.043047).
- [9] Tobias Hangleiter, Pascal Cerfontaine, and Hendrik Bluhm. “Erratum: Filter-function Formalism and Software Package to Compute Quantum Processes of Gate Sequences for Classical Non-Markovian Noise [Phys. Rev. Research 3, 043047 (2021)].” In: *Physical Review Research* 6.4 (Oct. 16, 2024), p. 049001. doi: [10.1103/PhysRevResearch.6.049001](https://doi.org/10.1103/PhysRevResearch.6.049001).
- [10] Isabel Nha Minh Le, Julian D. Teske, Tobias Hangleiter, Pascal Cerfontaine, and Hendrik Bluhm. “Analytic Filter-Function Derivatives for Quantum Optimal Control.” In: *Physical Review Applied* 17.2 (Feb. 2, 2022), p. 024006. doi: [10.1103/PhysRevApplied.17.024006](https://doi.org/10.1103/PhysRevApplied.17.024006).
- [11] Paul Surrey, Julian D. Teske, Tobias Hangleiter, Pascal Cerfontaine, and Hendrik Bluhm. “Data-Driven Qubit Characterization and Optimal Control Using Deep Learning.” In preparation.
- [12] Kui Wu, Sebastian Kindel, Thomas Descamps, Tobias Hangleiter, Jan Christoph Müller, Rebecca Rodrigo, Florian Merget, Beata E. Kardynał, Hendrik Bluhm, and Jeremy Witzens. “Modeling an Efficient Singlet-Triplet-Spin-Qubit-to-Photon Interface Assisted by a Photonic Crystal Cavity.” In: *Physical Review Applied* 21.5 (May 24, 2024), p. 054052. doi: [10.1103/PhysRevApplied.21.054052](https://doi.org/10.1103/PhysRevApplied.21.054052).
- [13] Kui Wu, Sebastian Kindel, Thomas Descamps, Tobias Hangleiter, Jan Christoph Müller, Rebecca Rodrigo, Florian Merget, Hendrik Bluhm, and Jeremy Witzens. “An Efficient Singlet-Triplet Spin Qubit to Fiber Interface Assisted by a Photonic Crystal Cavity.” In: *The 25th European Conference on Integrated Optics*. Ed. by Jeremy Witzens, Joyce Poon, Lars Zimmermann, and Wolfgang Freude. Cham: Springer Nature Switzerland, 2024, pp. 365–372. doi: [10.1007/978-3-031-63378-2\\_60](https://doi.org/10.1007/978-3-031-63378-2_60).

# Software

The following open-source software packages were developed (at least partially) during the work on this thesis.

- [1] Tobias Hangleiter, Isabel Nha Minh Le, and Julian D. Teske, *Filter\_functions* version v1.1.3, May 14, 2024. Zenodo. DOI: [10.5281/ZENODO.4575000](https://doi.org/10.5281/ZENODO.4575000),
- [2] Tobias Hangleiter, *Lindblad\_mc\_tools* Aug. 8, 2025. URL: [https://git.rwth-aachen.de/tobias.hangleiter/lindblad\\_mc\\_tools](https://git.rwth-aachen.de/tobias.hangleiter/lindblad_mc_tools).
- [3] Tobias Hangleiter, *Mjolnir* Aug. 8, 2025. URL: <https://git-ce.rwth-aachen.de/qutech/python-mjolnir>.
- [4] Tobias Hangleiter, Simon Humpohl, Max Beer, and René Otten, *Python-Spectrometer* version 2024.11.1, Nov. 21, 2024. Zenodo. DOI: [10.5281/ZENODO.13789861](https://doi.org/10.5281/ZENODO.13789861),
- [5] Tobias Hangleiter, Simon Humpohl, Paul Surrey, and Han Na We, *Qutil* version 2024.11.1, Nov. 21, 2024. Zenodo. DOI: [10.5281/ZENODO.14200303](https://doi.org/10.5281/ZENODO.14200303),

**Part I**

**A FLEXIBLE PYTHON TOOL FOR  
FOURIER-TRANSFORM NOISE  
SPECTROSCOPY**

**Author contributions** — *This part of the present thesis has benefited from discussions with several people as part of a course taught during the winter semester of 2022/23. The software package presented here was developed by me and has received contributions from Simon Humpohl,<sup>a</sup> Max Beer,<sup>a</sup> Paul Surrey,<sup>a</sup> and René Otten.<sup>b</sup>*

a: RWTH Aachen University and Forschungszentrum Jülich GmbH.

b: Then at RWTH Aachen University and Forschungszentrum Jülich.

**N**OISE is ubiquitous in condensed matter physics experiments, and in mesoscopic systems in particular it can easily drown out the sought-after signal. In solid-state quantum technology research, devices on the length scale of the Fermi wavelength – say tens of nanometers – are embedded in a crystalline matrix of  $10^{23}$  atoms. These devices host single quantum objects such as electrons or quasiparticles—collective many-body excitations. They are controlled and measured by classical signals routed to the device through macroscopic connections like cables and fibers. The signals, in turn, are generated and analyzed by electronic (e.g., transistors) or optical instruments (e.g., lasers) that, in all likelihood, are again based on solid-state technology driven by the first quantum revolution [1, 2]. Ultimately, then, the experiments take place in an environment full of external influences from trams passing by, shaking the ground, to cosmic rays creating electron-hole or breaking up Cooper pairs.

All of these different layers to such experiments are inherently – and in fact often fundamentally<sup>1</sup> – *noisy*, and it is the physicist’s challenge to measure their desired effects in spite of this noise. A well-thought-out experimental setup is hence one that has been designed taking the various noise sources into consideration, and state-of-the-art experiments often need to push the frontier in order to be successful. From material choice in the sample to the signal path and the specs of the measurement equipment, many aspects need to be optimized and, in particular, characterized in order to assess the noise. Indeed, the assessment of noise might even be the entire *goal* of the experiment, for instance to evaluate material properties. In this case, the quantity being measured might not be the same quantity whose noise one is interested in but rather some function of it, and the resulting data still needs to be transformed before one is able to make any practical statements about those properties.

Noise, in the sense that we are concerned with in the present thesis,<sup>2</sup> is a stochastic process, meaning that we cannot predict with certainty a dynamical system’s time evolution; it *fluctuates* randomly around its noise-free value.<sup>3</sup> Only by obtaining statistics, *i.e.*, repeated observations, either by preparing the system in the same initial state or measuring for a certain amount of time, can we make any statements about the underlying stochastic process. Two questions are key to assessing these statistics: first, what is the amplitude of the fluctuations? And second, at which frequency do the fluctuations occur? If the amplitude is small enough, we might not need to care, and if the frequency is large enough, we might be able to average out the fluctuations while if it is small enough, it might appear *quasistatic* and we might be able to subtract them. Although numerous other techniques for measuring and estimating a noise’s properties exist, analyzing noise in frequency space by means of the Fourier transform imposes itself when considering these two notions.

1: Consider Johnson-Nyquist noise in a resistor, for example.

2: Quantum noise does not fall under this scope as it may – disregarding vacuum fluctuations for the sake of argument – be considered *emergent*; it arises from a system entangled with a (not necessarily large) number of quantum degrees of freedom being observed, *i.e.*, tracing out the environment’s degrees of freedom. Our lack of knowledge about this environment then appears as noise in our observations. See Reference 3 for a comprehensive review of the quantum case.

3: Quantum measurements are also noisy in this sense as we cannot predict the outcome of a single-shot measurement, but here the stochasticity is in the outcomes of an ensemble rather than the sequence of values in time. The two are, however, closely related through ergodicity, which we will require in Section 2.1.

This approach is the central topic of this part of the present thesis. However, we will not be too much concerned with the theoretical side of the subject matter. Rather, I will focus on making these techniques readily and easily accessible to experimentalists in the lab. Given the arguments laid out above, noise spectroscopy should be an essential item in an experimentalists toolbelt. In practice, though, we are faced with several challenges. First, different experiments require different data acquisition (DAQ) hardware, all of which have both varying capabilities and software interfaces. Hence, transferring a spectroscopy code from one device or setup to another is a non-trivial task and can inhibit adoption of the technique. Albeit some instruments come with built-in spectroscopy solutions, they vary in functionality and are not easily transferred to different systems. Second, while probably everyone finding themselves in the situation is capable of computing the noise spectrum when presented with a set of time series data, inferring the correct parameters for data acquisition given the desired parameters of the resulting spectrum can, while not difficult, be cumbersome to do.<sup>4</sup> Lastly, noise spectroscopy is most effective when proper visualization tools are employed. Again, this is not a difficult task per se, but such things always incur overhead costs that can deter users from employing these essential techniques.

Here, I address these points by introducing a Python software package, `python_spectrometer` [4], that tackles the entire processing chain of practical noise spectroscopy in a physics laboratory. By abstracting DAQ hardware into a unified interface, it is portable between different setups. With the goal to make noise spectroscopy as accessible as possible and lower the entry barrier, it automatically handles parameter inference and hardware constraints. Finally, it provides a comprehensive plotting solution that allows for interactively analyzing the data using various different data visualization methods.

The rest of this part is structured as follows. In Chapter 2, I review the mathematical groundwork underpinning noise spectroscopy by means of Fourier transforms of time series and discuss parameters and properties of the central quantity of interest, the power spectral density (PSD). In Chapter 3, I then present the software package by going over its design choices and giving a walkthrough of its features using a typical workflow as an example. I conclude by giving an outlook on future directions in Chapter 4.

4: Although it is of course a good exercise, and, as a physicist, one should always strive to understand the tools one is using and the underlying principles at work. This part of the present thesis is intended to provide a starting point for that.

# Theory of spectral noise estimation

2

THERE exist various methods for estimating the properties of noise in a classical signal  $x(t)$ .<sup>1</sup> A simple metric quantifying the average noise amplitude of the signal observed from time  $t = 0$  to  $t = T$  is the root mean square (RMS) [6],

$$\text{RMS}_x = \sqrt{\frac{1}{T} \int_0^T dt |x(t)|^2}. \quad (2.1)$$

While this already tells us *something* about the noise, it is evident that a single number does not provide many clues if we were to attempt to mitigate the noise or say something qualitative about it beyond “small” and “large”. In cases such as these, physics has often turned to the *spectral* representation of the function of interest. Knowing the frequency content of a function gives access to a wealth of information about the underlying contributing processes. But how can we learn how a system behaves as a function of frequency?

Consider an electrical black box – some device under test (DUT) – with two leads connected to a lock-in amplifier (LIA) as sketched in Figure 2.1. Assuming the DUT is conducting, we could simply measure the conductance  $G(t) = I(t)/V(t)$  through the device for some time  $T$  with a given lock-in modulation frequency  $f_i$ , subtract the constant offset,<sup>2</sup> and calculate the RMS using Equation 2.1. Repeating this procedure for different modulation frequencies  $\{f_i\}$ , we would collect a set of RMS-values that we could assign to the modulation frequencies at which they were measured and thus sample the noise amplitude spectrum<sup>3</sup> of the conductance,  $S_G(f_i)$ .<sup>4</sup> This method has the advantage that we can choose the frequencies at which the spectrum should be sampled—in particular they do not have to be evenly spaced. However, it has two significant shortcomings. First, it is rather inefficient and therefore time-consuming. For  $N$  frequency sample points, it takes a total time of  $NT$  to acquire all data, where  $T$  needs to be chosen such that the variance of  $\text{RMS}_G$  is sufficiently small. Second, and crucially, it is not always possible to excite the system at a certain frequency and measure its response. For example, it is generally considered hard<sup>5</sup> to – deliberately – excite vibrations of a specific frequency in a cryostat, yet we might still be interested in the displacement spectrum inside of it. A related method is available if one has access to a frequency-tunable probe, that is, a physical system whose behavior – typically its time evolution or some measurable property after letting the system evolve – under noise is well understood within a given noise model, and that can be controlled to be sensitive to a certain frequency. One example for such methods is dynamical decoupling (DD)-based noise spectroscopy using a qubit [7–10], a protocol based on insights gained from the filter-function formalism—see Part IV. These protocols are especially well-suited for high but less so for low frequencies as they rely on observing the coherence of a qubit and hence the visibility on long time scales.

In a sense the most straight-forward way of measuring the noise spectrum presents itself as a consequence of the Wiener-Khinchin theorem [11, 12] that relates the noise spectrum to the Fourier transform of a time-dependent signal. This makes it possible to estimate the noise spectrum by simply observing a signal for a certain amount of time and perform-

1: We discuss only classical noise here, meaning  $x(t)$  commutes with itself at all times. For descriptions of and spectroscopy protocols for quantum noise refer to References 3 and 5, for example.

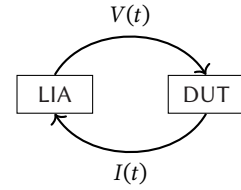


**Figure 2.1:** Measuring the conductance through a device under test (DUT) using a lock-in amplifier (LIA).

2: The constant part  $G_0 = G(t) - \delta G(t)$  of course also holds some information about the system, for example about its bandwidth.

3: We will properly define this term below.

4: See Subsection 3.2.1 for a discussion on how the RMS at a certain frequency relates to other quantities discussed in this part.

5: And also unpopular with colleagues.



ing some post-processing!<sup>6</sup> This method will be the topic of the present chapter. It is laid out as follows. I will first derive the Wiener-Khinchin theorem for continuous stochastic processes and introduce the central quantity of interest in noise spectroscopy; the PSD. Then, I will discretize the method and discuss resulting side-effects before describing an efficient way of obtaining the spectrum from a finite amount of data. I will conclude by elaborating on relevant parameters and properties.

## 2.1 Spectrum estimation from time series

To see how spectral noise properties may be estimated from time series data, consider a continuous wide-sense stationary<sup>7</sup> signal in the time domain,  $x(t) \in \mathbb{C}$ , that is observed for some time  $T$ . We define the windowed Fourier transform of  $x(t)$  and its inverse by<sup>8</sup>

$$\hat{x}_T(\omega) = \int_0^T dt x(t) e^{-i\omega t} \quad (2.2)$$

$$x(t) = \int_{-\infty}^{\infty} \frac{d\omega}{2\pi} \hat{x}_T(\omega) e^{i\omega t}, \quad (2.3)$$

i.e., we assume that outside of the window of observation  $x(t)$  is zero. The autocorrelation function of  $x(t)$  is given by

$$C(\tau) = \langle x^*(t) x(t + \tau) \rangle \quad (2.4)$$

$$= \lim_{T \rightarrow \infty} \frac{1}{T} \int_0^T dt x^*(t) x(t + \tau), \quad (2.5)$$

where  $\langle \cdot \rangle$  is the ensemble average over multiple realizations of the process and the last equality holds true for ergodic processes. Expressing  $x(t)$  in terms of its Fourier representation (Equation 2.2) and reordering the integrals, we get

$$C(\tau) = \lim_{T \rightarrow \infty} \frac{1}{T} \int_0^T dt \int_{-\infty}^{\infty} \frac{d\omega}{2\pi} \hat{x}_T^*(\omega) e^{-i\omega t} \int_{-\infty}^{\infty} \frac{d\omega'}{2\pi} \hat{x}_T(\omega') e^{i\omega'(t+\tau)} \quad (2.6)$$

$$= \lim_{T \rightarrow \infty} \frac{1}{T} \int_{-\infty}^{\infty} \frac{d\omega}{2\pi} \int_{-\infty}^{\infty} \frac{d\omega'}{2\pi} \hat{x}_T^*(\omega) \hat{x}_T(\omega') e^{i\omega'\tau} \int_0^T dt e^{it(\omega' - \omega)} \quad (2.7)$$

The innermost integral approaches a  $\delta$ -function for large  $T$ , allowing us to further simplify this under the limit as<sup>9</sup>

$$C(\tau) = \lim_{T \rightarrow \infty} \frac{1}{T} \int_{-\infty}^{\infty} \frac{d\omega}{2\pi} \int_{-\infty}^{\infty} \frac{d\omega'}{2\pi} \hat{x}_T^*(\omega) \hat{x}_T(\omega') e^{i\omega'\tau} \delta(\omega' - \omega) \quad (2.8)$$

$$= \lim_{T \rightarrow \infty} \frac{1}{T} \int_{-\infty}^{\infty} \frac{d\omega}{2\pi} |\hat{x}_T(\omega)|^2 e^{i\omega\tau} \quad (2.9)$$

$$= \int_{-\infty}^{\infty} \frac{d\omega}{2\pi} S(\omega) e^{i\omega\tau} \quad (2.10)$$

with the power spectral density (PSD)<sup>10</sup>

$$S(\omega) = \lim_{T \rightarrow \infty} \frac{1}{T} |\hat{x}_T(\omega)|^2 \quad (2.11)$$

$$= \int_{-\infty}^{\infty} d\tau C(\tau) e^{-i\omega\tau} \quad (2.12)$$

6: An interesting combination of the Fourier-transform-based and the qubit-based spectroscopy methods was recently proposed in Reference 13, where the authors compute the spectrum by Fourier-transforming the second derivative of the coherence function.

7: For a wide-sense stationary (also called weakly stationary) process  $x(t)$ , the mean is constant and the autocorrelation function  $C(t, t') = \langle x^*(t) x(t') \rangle$  simplifies to  $\langle x^*(t) x(t + \tau) \rangle = \langle x^*(0) x(\tau) \rangle$  with  $\tau = t' - t$  and where  $\langle \cdot \rangle$  is the ensemble average. That is, it is a function of only the time lag  $\tau$  and not the absolute point in time. For Gaussian processes as discussed here, this also implies stationarity [14]. The property further implies that  $C(\tau)$  is an even function.

8: In this chapter we will always denote the Fourier transform of some quantity  $\xi$  using the same symbol with a hat,  $\hat{\xi}$ .

9: We normalize the  $\delta$ -function such that  $1 = \int \frac{d\omega}{2\pi} \delta(\omega)$ .

10: The term *power spectrum* is often used interchangeably. I will do so as well, but emphasize at this point that in digital signal processing in particular, the *spectrum* is a different quantity from the *spectral density*. See also Sidenote 20 in Chapter 3.



Equation 2.10 is the Wiener-Khinchin theorem [11, 12] that states that the autocorrelation function  $C(\tau)$  and the PSD  $S(\omega)$  are Fourier-transform pairs [14]. Furthermore, defining the latter through Equation 2.11 gives us an intuitive picture of the PSD if we recall Parseval's theorem,

$$\int_{-\infty}^{\infty} \frac{d\omega}{2\pi} \frac{1}{T} |\hat{x}_T(\omega)|^2 = \frac{1}{T} \int_0^T dt |x(t)|^2. \quad (2.13)$$

That is, the total power  $P$  contained in the signal  $x(t)$  is given by integrating over the PSD. Similarly, the power contained in a band of frequencies  $[\omega_1, \omega_2]$  is given by

$$P(\omega_1, \omega_2) = \text{RMS}_S(\omega_1, \omega_2)^2 \quad (2.14)$$

$$= \int_{\omega_1}^{\omega_2} \frac{d\omega}{2\pi} S(\omega) \quad (2.15)$$

where  $\text{RMS}_S(\omega_1, \omega_2)$  is the root mean square within this frequency band. These relations are helpful when analyzing noise PSDs to gauge the relative weight of contributions from different frequency bands to the total noise power.

To become familiar with the quantities  $C(\tau)$  and  $S(\omega)$ , consider the Ornstein-Uhlenbeck process [15], the only stationary Gaussian Markovian stochastic process [16]. The autocorrelation function of the Ornstein-Uhlenbeck process is given by

$$C(\tau) = \sigma^2 e^{-\tau/\tau_c}, \quad (2.16)$$

with  $\sigma$  the RMS and  $\tau_c$  the correlation time of the process. The PSD in turn is the Lorentzian function

$$S(\omega) = \frac{2\sigma^2\tau_c}{1 + (\omega\tau_c)^2}. \quad (2.17)$$

For a given discretization time step  $\Delta t$  and hence bandwidth  $\omega \in [0, \pi f_s]$ , the Ornstein-Uhlenbeck process interpolates between perfectly uncorrelated, white noise ( $\Delta t/\tau_c \rightarrow \infty, S(\omega) = 2\tau_c\sigma^2$ ), correlated, Brownian noise ( $\Delta t/\tau_c \gg 1, S(\omega) = 2\sigma^2/\tau_c\omega^2$ ), and perfectly correlated, quasistatic noise ( $\Delta t/\tau_c \rightarrow 0, S(\omega) = \sigma^2\delta(\omega)$ ), although I note that it is still Markovian in all cases. Figure 2.2 depicts simulated data and its autocorrelation function and PSD for exemplary parameters: in the white noise limit ( $\tau_c = 10^{-2}\Delta t$ , blue), in the intermediate regime ( $\tau_c = \Delta t$ , magenta), and in the correlated regime ( $\tau_c = 10^2\Delta t$ , green). From the time series plot at the top it becomes clear that the RMS alone is insufficient to describe the properties of noisy signals as the curves differ significantly despite being normalized to their RMS. The autocorrelation functions averaged over  $10^3$  realizations of the noisy signals as well as their theoretical (continuous) value, Equation 2.16, are plotted in the middle panel, normalized to  $\tau_c = \Delta t$  and  $\sigma^2 = \Delta t/4$ . For the white noise limit (blue), correlations are too short to be resolved with the given time discretization. The correlations decay to  $e^{-1}$  at  $\tau/\tau_c = 10^{-2}, 1, 10^2$ , respectively. Finally, the bottom panel shows the PSD, Equation 2.17, and its periodogram estimate, again averaged over  $10^3$  realizations of the signal and normalized to  $\tau_c = \Delta t$  and  $\sigma^2 = \Delta t/4$ . The cross-over from white to Brownian PSD occurs at  $\omega = \tau_c$ . While the simulated data for  $\tau_c = 10^{-2}\Delta t$  appears perfectly white, that for  $\tau_c = 10^2\Delta t$  appears perfectly  $1/f$ -like because the spectrum is only white below the smallest resolvable frequency  $\Delta f = T^{-1}$ .

Having gotten an intuition for the quantities  $C(\tau)$  and  $S(\omega)$ , let us move

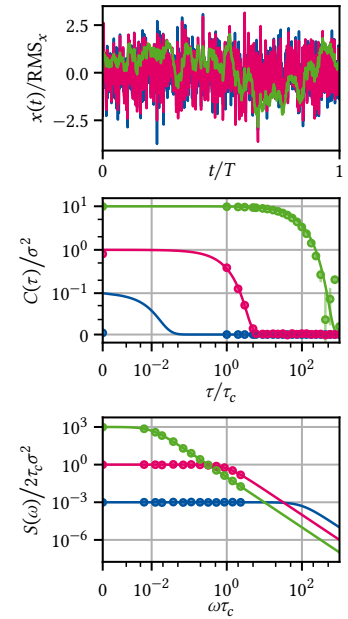


**Figure 2.2:** Ornstein-Uhlenbeck process. Simulated time traces, autocorrelation function, and PSD of the Ornstein-Uhlenbeck process. Top: Simulated time traces using the algorithm presented in Section A.4. The data are normalized to the computed RMS (equal to  $\sigma$  in the continuous case). Middle: Theoretical autocorrelation function (Equation 2.16, solid lines) computed from the simulated data averaged over  $10^3$  traces (circles, subset of points). Error bars indicate the standard error of the mean, axes are scaled with respect to the parameters of the magenta data, and data are plotted on an asinh-scale. Bottom: Theoretical PSD (Equation 2.17, solid lines) and periodograms computed from the simulated data using `scipy.signal.periodogram()`, cf. Equation 2.21, averaged over  $10^3$  traces (circles, subset of points). Axes are again scaled with respect to the parameters of the magenta data and plotted on an asinh-scale. Parameters are  $\tau_c = \Delta t \times \{10^{-2}, 1, 10^2\}$  and  $\sigma^2 = \sqrt{\tau_c}/4$  for blue, magenta, and green data, respectively.

on to see how the latter may be obtained from time series data. Equation 2.11 represents the starting point for the experimental spectrum estimation procedure. Instead of a continuous signal  $x(t), t \in [0, T]$ , consider its discretized version<sup>11</sup>

$$x_n, \quad n \in \{0, 1, \dots, N-1\} \quad (2.18)$$

defined at times  $t_n = n\Delta t$  with  $T = N\Delta t$  and where  $\Delta t = f_s^{-1}$  is the sampling interval (the inverse of the sampling frequency  $f_s$ ). Invoking the ergodic theorem,<sup>12</sup> we can replace the long-term average in Equation 2.11 by the ensemble average over  $M$  realizations of the noisy signal,  $\{x_n^{(m)}\}_m$ , and write

$$S_n = \frac{1}{M} \sum_{m=0}^{M-1} |\hat{x}_n^{(m)}|^2 \quad (2.19)$$

$$= \frac{1}{M} \sum_{m=0}^{M-1} S_n^{(m)} \quad (2.20)$$

where  $\hat{x}_n^{(m)}$  is the discrete Fourier transform of  $x_n^{(m)}$ , we defined the *periodogram* of  $x_n^{(m)}$  by

$$S_n^{(m)} = |\hat{x}_n^{(m)}|^2, \quad (2.21)$$

and  $S_n$  is an *estimate* of the true PSD sampled at the discrete frequencies  $\omega_n = 2\pi n/T \in 2\pi \times \{-f_s/2, \dots, f_s/2\}$ . Equation 2.19 is known as Bartlett's method [19] for spectrum estimation.<sup>13</sup>

To better understand the properties of this estimate, let us take a look at the parameters  $\Delta t$ ,  $N$ , and  $M$ . The sampling interval  $\Delta t$  defines the largest resolvable frequency by the Nyquist sampling theorem,

$$f_{\max} = \frac{f_s}{2} = \frac{1}{2\Delta t}. \quad (2.22)$$

In turn, the number of samples  $N$  determines the frequency resolution  $\Delta f$ , or smallest resolvable frequency,

$$f_{\min} = \Delta f = \frac{1}{T} = \frac{1}{N\Delta t} = \frac{f_s}{N}. \quad (2.23)$$

Lastly,  $M$  determines the variance of the set of periodograms  $\{S_n^{(m)}\}_{i=0}^{M-1}$  and hence the accuracy of the estimate  $S_n$ .

In practice, the ensemble realizations  $i$  are of course obtained sequentially, implying that one acquires a time series of data  $x_n, n \in \{0, 1, \dots, NM-1\}$  and partitions these data into  $M$  sequences of length  $N$ . It becomes clear, then, that the Bartlett average (Equation 2.19) trades spectral resolution (larger  $N$ ) for estimation accuracy (larger  $M$ ) given the finite acquisition time  $T = NM\Delta t$ . An improvement in data efficiency can be achieved using Welch's method [20]. To see how, we first need to discuss spectral windowing.

## 2.2 Window functions

Partitioning a signal  $x_n$  into  $M$  sections  $x_n^{(m)}$  of length  $N$  is mathematically equivalent to multiplying the signal with the rectangular *window*

11: We only discuss the problem of equally spaced samples here. Variants for spectral estimation of time series with unequal spacing exist [17, 18].

12: Note that the limit of perfectly correlated noise,  $S(\omega) \propto \delta(\omega)$ , technically does *not* correspond to an ergodic process because  $C(\tau) = \text{const. } \forall \tau \in (-\infty, \infty)$ . In practice, this is always a mathematical idealization and the spectrum is actually better described by a nascent  $\delta$ -function with a small but finite width.

13: By taking the limit  $M \rightarrow \infty$  one recovers the true PSD,

$$\lim_{M \rightarrow \infty} S_n = S(\omega_n).$$

The continuum limit is as always obtained by sending  $\Delta t \rightarrow 0, N \rightarrow \infty, N\Delta t = \text{const.}$

function given by<sup>14</sup>

$$w_n^{(m)} = \begin{cases} 1 & \text{if } (m-1)N \leq n < mN \text{ and} \\ 0 & \text{else} \end{cases} \quad (2.24)$$

so that  $x_n^{(m)} = x_n w_n^{(m)}$ . Now recall that multiplication and convolution are duals under the Fourier transform, implying that

$$\hat{x}_n^{(m)} = \hat{x}_n * \hat{w}_n^{(m)}, \quad (2.25)$$

where the Fourier representation of the rectangular window is given by<sup>15</sup>

$$\hat{w}_n^{(m)} = \hat{w}_n e^{-i(m-1/2)\omega_n T}, \quad (2.26)$$

$$\hat{w}_n = T \operatorname{sinc}\left(\frac{\omega_n T}{2}\right). \quad (2.27)$$

Figure 2.3 shows the unshifted rectangular window  $\hat{w}_n$  in Fourier space. We can hence understand the Fourier spectrum of  $x_n^{(m)}$  as sampling  $\hat{x}_n$  with the probe  $\hat{w}_n^{(m)}$ . However, whereas in the continuum limit (see Side-note 13) Equation 2.27 tends towards  $\delta(\omega_n)$  and thus will produce a faithful reconstruction of the true spectrum, the finite sample rate  $f_s$  of discrete signals and observation length  $T$  induce finite frequency sampling and bandwidth of the probe as well as *sidelobes*.<sup>16</sup> These effects incur what is known as *spectral leakage* and *scalping loss*, respectively, and lead to artifacts and deviations of the spectrum estimator  $S_n$  from the true spectrum  $S(\omega_n)$  [14, 21].

For this reason, a plethora of *window functions* have been introduced to mitigate the effects of spectral leakage. Key properties of a window are the spectral bandwidth (center lobe width) and sidelobe amplitude between which there typically is a tradeoff.<sup>17</sup> A window frequently used in spectral analysis is the Hann window [23],

$$w_n^{(m)} = \begin{cases} \sin^2\left(\frac{\pi n}{N}\right) & \text{if } (m-1)N \leq n < mN \text{ and} \\ 0 & \text{else,} \end{cases} \quad (2.28)$$

with the Fourier representation of the unshifted window,

$$\hat{w}_n = \frac{T}{2} \operatorname{sinc}\left(\frac{\omega_n T}{2}\right) \frac{1}{1 - (\omega_n T/2\pi)^2} \quad (2.29)$$

shown in Figure 2.4. The favorable properties of the Hann window are apparent when compared to the rectangular window in Equation 2.27 and Figure 2.3; the sidelobes are quadratically suppressed while the center lobe is broadened by a factor of two.

Another favorable property of the Hann window is that  $w_0^{(0)} = w_{N-1}^{(0)} = 0$ . This suppresses detrimental effects arising from a possible discontinuity ( $x_0^{(0)} \neq x_{N-1}^{(0)}$ ) at the edge of a data segment related to the discrete Fourier transform, which assumes periodic data.<sup>18</sup>

14: This window is also known as the boxcar or Dirichlet window.

15:  $\operatorname{sinc}(x) = \sin(x)/x$ .

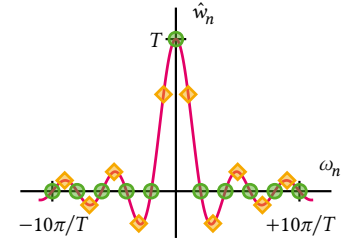


**Figure 2.3:** The Fourier representation of the rectangular window in continuous time (solid line) and for discrete frequencies  $\omega_n = 2\pi n/T$  (circles). Introducing a phase shift, that is, shifting the window with respect to the signal in time, effectively shifts  $\omega_n \rightarrow \omega_n + \eta$  as indicated for  $\eta = 1/2$  (diamonds). This incurs scalping loss.

16: For the optically inclined: this is akin to Fraunhofer diffraction at an aperture.

17: Wikipedia gives a good overview of existing window functions [22].

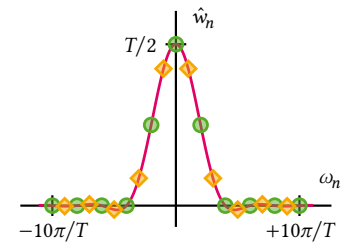


**Figure 2.4:** The Fourier representation of the Hann window in continuous time (solid line) and for discrete frequencies  $\omega_n$  (circles). Diamonds indicate discrete sampling when the window completely out of phase with the signal (cf. Figure 2.3).

18: Although this can usually also be achieved approximately by detrending

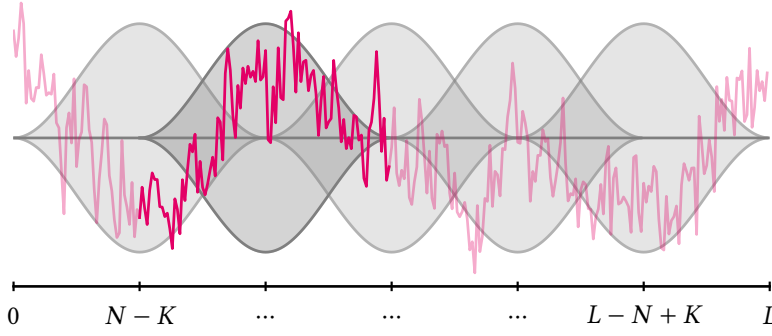


**Figure 2.5:** Illustration of Welch's method for spectrum estimation. The data (magenta) of length  $L$  is partitioned into  $K = 2L/N - 1$  segments of length  $N$ . Each segment is multiplied with a window function (gray) which reduces spectral leakage and other artifacts. A finite overlap  $K$  between adjacent windows (gray) ensures efficient sample use.

## 2.3 Welch's method

Contemplating Equation 2.28, one might come to the conclusion that using a window such as this is not very data efficient in the sense that a large fraction of samples located at the edge of the window is strongly suppressed and hence does not contribute significantly to the spectrum estimate. To alleviate this lack of efficiency, one can introduce an overlap between adjacent data windows. That is, instead of partitioning the data  $x_n$  into  $M$  non-overlapping sections of length  $N$ , one shifts the  $m$ th window backward by  $mK$  with  $K > 0$  the overlap. Finally, the periodogram (Equation 2.21) is computed for each window and subsequently averaged to obtain the spectrum estimator (Equation 2.19).

This method of spectrum estimation is known as Welch's method [20]. One can show [20] that the correlation between the periodograms of adjacent, overlapping windows is sufficiently small to avoid a biased estimate. The overlap naturally depends on the choice of window; a typical value for the Hann window  $K = N/2$  with which one would obtain  $M = 2L/N - 1$  windows for data of length  $L$ .<sup>19</sup>

Figure 2.5 conceptually illustrates Welch's method for a trace of  $1/f$  noise with  $L = 300$  samples in total. Choosing the Hann window and an overlap of 50% results in  $M = 5$  segments for a window length of  $N = 100$ . The data in the second window is highlighted.

## 2.4 Parameters & Properties of the PSD

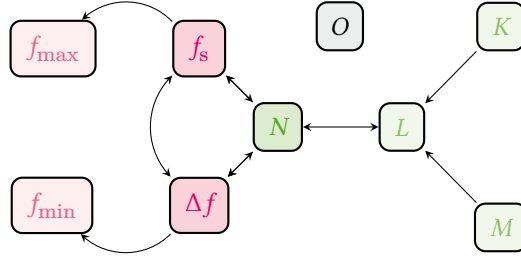
We are now in a position to discuss how the various parameters of a time series relate to both the physical parameters of the resulting spectrum estimate and to each other. To this end, we will go through the typical procedure of acquiring a spectrum estimate using Welch's method chronologically. Table 2.1 gives an overview of all relevant parameters.

To acquire data using some form of (digital) DAQ, one usually needs to specify two parameters first: the total number of samples to be acquired,  $L$ , and the sample rate  $f_s$ . This results in a measurement of duration  $T = L\Delta t$  where  $\Delta t = f_s^{-1}$  as previously mentioned. The choice of  $f_s$  already induces an upper bound on the first parameter characterizing the PSD estimate: the largest resolvable frequency  $f_{\max} \leq f_s/2$  (cf. Equation 2.22, but note that we allow  $f_{\max}$  to be smaller than half the sample rate in anticipation of hardware constraints). Next, we choose a number of Welch averages,  $M$ , i.e., data partitions, and their overlap,  $K$ . In doing so, one fixes the number of samples per partition  $N$  and thereby induces

19: Again neglecting integer arithmetic issues.

**Table 2.1:** Overview of spectrum estimation parameters. The parameters can be assigned into four groups: 1. DAQ parameters configuring the data acquisition device, 2. Welch parameters specifying the periodogram averaging, 3. Spectrum properties induced by the above, and 4. External parameters unrelated to the others.

1. DAQ PARAMETERS	
$L$	Total number of samples
$f_s$	Sample rate
2. WELCH PARAMETERS	
$K$	Number of overlap samples
$N$	Number of segment samples
$M$	Number of Welch segments
3. SPECTRUM PARAMETERS	
$f_{\min}$	Smallest resolvable frequency
$f_{\max}$	Largest resolvable frequency
4. MISCELLANEOUS PARAMETERS	
$O$	Number of outer averages



the lower bound on the second parameter characterizing the PSD estimate: the frequency spacing  $\Delta f = 1/N \leq f_{\min}$  (cf. Equation 2.23).<sup>20</sup> Finally, we can introduce a number of *outer* averages  $O$ , that is, the number of data batches that are acquired. While not directly related to Welch's method, choosing  $O > 1$  can, for instance, help achieve a certain variance if the number of samples per batch,  $L$ , is limited by the data acquisition hardware, or simply allow for updating the spectrum estimate as data is being acquired. Figure 2.6 shows the relationships of the various parameters among each other. In Subsection 3.1.1, I lay out how these inter-dependencies are implemented in software.

To conclude this chapter, let us discuss some of the properties of stochastic processes and their autocorrelation function and PSD. Consider again the process  $x(t)$ . We say  $x(t)$  is *Gaussian* if  $x(t) \sim \mathcal{N}(\mu, \sigma^2) \forall t$ , meaning that the value of  $x(t)$  at a given point in time follows a normal distribution with some mean  $\mu$  and variance  $\sigma^2$  over multiple realizations of the process. In this case, its statistical properties are fully described by the autocorrelation function  $C(\tau)$  and PSD  $S(\omega)$ . This is because only the first two cumulants of a Gaussian distribution are nonzero [24]. For the purpose of noise estimation, the assumption of Gaussianity is a rather weak one as the noise typically arises from a large ensemble of individual fluctuators and is therefore well approximated by a Gaussian distribution by the central limit theorem [25].<sup>21</sup> Even if  $x(t)$  is not perfectly Gaussian, non-Gaussian contributions can be seen as higher-order contributions if viewed from the perspective of perturbation theory, and therefore the PSD still captures a significant part of the statistical properties. For this reason, the PSD is the central quantity of interest in noise spectroscopy. Let us just note at this point that techniques to estimate higher-order spectra (or *polyspectra*) exist [8, 29–31].

For real signals  $x(t) \in \mathbb{R}$ , the autocorrelation function  $C(\tau)$  is an even function, while for  $x(t) \in \mathbb{C}$  its real part is even and its complex part odd. From this it immediately follows that for real  $x(t)$   $S(\omega)$  is also an even function and one therefore distinguishes the *two-sided* PSD  $S^{(2)}(\omega)$  defined over  $\mathbb{R}$  from the *one-sided* PSD  $S^{(1)}(\omega) = 2S^{(2)}(\omega)$  defined only over  $\mathbb{R}^+$ . Complex  $x(t)$  such as those generated by LIAs after demodulation in turn have asymmetric, two-sided PSDs. In this chapter so far, we have implicitly employed the two-sided definition, but in the software package presented in Chapter 3, two-sided spectra are used only for complex data since they contain redundant information for real data.

**Figure 2.6:** Relationships of data acquisition parameters (cf. Tables 2.1 and 3.1, with arrows indicating dependencies.  $N$ ,  $f_s$ , and  $\Delta f$  are the central quantities defining the estimated spectrum's properties (darker shades). From  $f_s$  and  $\Delta f$  follow (bounds for)  $f_{\max}$  and  $f_{\min}$  (shaded red, rational numbers). From  $N$ , together with  $K$  and  $M$ , follows  $L$ , the total number of samples per data batch (shaded green, integers).

<sup>20</sup>: Technically, the smallest resolvable frequency in a fast Fourier transform (FFT) is zero, of course. But as data is typically detrended (a constant or linear trend subtracted) before computation of the periodogram, the smallest *meaningful* frequency is given by  $f_{\min}$ .

<sup>21</sup>: As an example, consider electronic devices, where voltage noise is thought to arise from a large number of defects and other charge traps in oxides being populated and depopulated at certain rates  $\gamma$ . The ensemble average over these so-called two-level fluctuators (TLFs) then yields the well-known  $1/f$ -like noise spectra [26, 27] (at least for a large density [28]).



# The `python_spectrometer` software package

3

In this chapter, I introduce the `python_spectrometer` Python package<sup>1</sup> [4] and lay out its design and functionality. This software package was developed to make it easier for experimentalists to transfer the mathematical machinery introduced in Chapter 2 to the lab. While in principle the entire process of spectrum estimation from a given array of time series data is already covered by the `welch()` routine in SciPy [32], obtaining the data array is not standardized. Different DAQ instruments have different capabilities, both on the hardware and the software level, and different driver interfaces to communicate with them. This implies that custom data acquisition code is required for every instrument, introducing a significant entry barrier to spectral analysis. The `python_spectrometer` package implements a simple interface to different hardware instruments that allows for changing the hardware backend without having to adapt the user-facing code and also incorporates different hardware constraints.

What is more, noise spectroscopy tends to be a visual endeavor in practice; it is hard to compare different noise spectra based on quantitative reasoning alone. Data visualization is hence an integral part of noise spectroscopy, but plotting is not just plotting. Do we want the data to be shown on a log-log scale?<sup>2</sup> Do we want to show the relative magnitude of different data sets? Do we want to inspect the time traces as well? The `python_spectrometer` package addresses these questions by allowing users to interactively change features of the main plot window to adapt it to the form best suited to the situation at hand.

Moreover, when concerned with noise spectrum estimation, we are typically more interested in specifying parameters of the resulting PSD rather than parameters of the underlying time series data. The `python_spectrometer` package approaches data acquisition from the inverse direction: rather than inferring the spectrum properties from the time series data, users specify the properties they would like the resulting spectrum to have and the package chooses the correct parameters for data acquisition accordingly.

## 3.1 Package design and implementation

The `python_spectrometer` package provides a central class, `Spectrometer`, that users interact with to perform data acquisition, spectrum estimation, and plotting. It is instantiated with an instance of a child class of the DAQ base class that implements an interface to various DAQ hardware devices.<sup>3</sup> New spectra are obtained by calling the `Spectrometer.take()` method with all acquisition and metadata settings. In the following, I will go over the the design of these aspects of the package in more detail.

### 3.1.1 Data acquisition

Figure 3.1 shows the directory structure of the source code. The `daq` subpackage contains on the one hand the declaration of the DAQ abstract base class (`base.py`) and its child class implementations (`qcodes.py`, *etc.*), and on the other the `settings.py` module, which defines the `DAQSettings`

1: The package repository is hosted on [GitLab](#). Its documentation is automatically generated and hosted on [GitLab Pages](#). Releases are automatically published to [PyPI](#) and allow the package to be installed using `pip install python-spectrometer`.

2: The short answer is yes, but it comes with visual side-effects that demand other ways of plotting data at times. The long answer is therefore yes, and ...

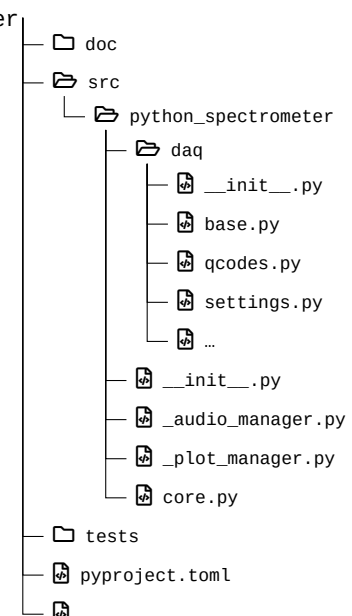


**Figure 3.1:** Source tree structure of the `python_spectrometer` package. Driver wrappers are placed in the `daq` subpackage. `core.py` exports the `Spectrometer` class.

3: Actually *drivers* to be more precise.

class. This class is used in the background to validate data acquisition settings both for consistency (see Section 2.4) and hardware constraints.

To better understand the necessity of this functionality, consider the typical scenario of a physicist<sup>4</sup> in the lab. Alice has wired up her experiment, performed a first measurement, and to her dismay discovered that the data is too noisy to see the sought-after effect. She sets up the `python_spectrometer` code to investigate the noise spectrum of her measurement setup. From her noisy data she could already estimate the frequency of the most harrowing noise, so she knows the frequency band  $[f_{\min}, f_{\max}]$  she is most interested in. But because she is lazy, she does not want to do the mental gymnastics to convert  $f_{\min}$  to the parameter that her DAQ device understands,  $L$  (see Table 3.1), especially considering that  $L$  depends on the number of Welch averages and the overlap. Furthermore, while she could just about do the conversion from  $f_{\max}$  to the other relevant DAQ parameter,  $f_s$ , in her head, her device imposes hardware constraints on the allowed sample rates she can select! The `DAQSettings` class addresses these issues. It is instantiated with any subset of the parameters listed in Table 3.1<sup>5</sup> and attempts to resolve the parameter interdependencies laid out in Section 2.4 and depicted in Figure 2.6 upon calling `DAQSettings.to_consistent_dict()`.<sup>6</sup> This either infers those parameters that were not given from those that were or, if not possible, uses a default value. Child classes of the DAQ class can subclass `DAQSettings` to implement hardware constraints such as a finite set of allowed sampling rates or a maximum number of samples per data buffer.

For instance, Alice might want to measure the noise spectrum in the frequency band [1.5 Hz, 72 kHz]. Although she would not have to do this explicitly,<sup>7</sup> she could inspect the parameters after resolution using the code shown in Listing 3.1.

```
>>> from python_spectrometer.daq import DAQSettings
>>> settings = DAQSettings(f_min=1.5, f_max=7.2e4)
>>> settings.to_consistent_dict()
{'f_min': 1.5,
 'f_max': 72000.0,
 'fs': 144000.0,
 'df': 1.5,
 'nperseg': 96000,
 'noverlap': 48000,
 'n_seg': 5,
 'n_pts': 288000,
 'n_avg': 1}
```

If the instrument she'd chosen for data acquisition had been a Zurich Instruments MFLI's Scope module,<sup>8</sup> the same requested settings would have resolved to those shown in Listing 3.2.<sup>9</sup> This is because the Scope module constrains  $L \in [2^{12}, 2^{14}]$  and  $f_s \in 60 \text{ MHz} \times 2^{[-16,0]} \approx \{915.5 \text{ Hz}, \dots, 30 \text{ MHz}, 60 \text{ MHz}\}$ .

As already mentioned, the DAQ base class implements a common interface for different hardware backends, allowing the `Spectrometer` class to be hardware-agnostic. That is, changing the instrument that is used to acquire the data does not necessitate adapting the code used to interact with the `Spectrometer`. To enable this, different instruments require small wrapper drivers that map the functionality of their actual driver onto the interface dictated by the DAQ class. This is achieved by subclassing `DAQ` and implementing the `DAQ.setup()` and `DAQ.acquire()` meth-

**Table 3.1:** Variable names used in Chapter 2 and their corresponding parameter names as used in `python_spectrometer` and `scipy.signal.welch()` [32].

VARIABLE	PARAMETER
$L$	<code>n_pts</code>
$N$	<code>nperseg</code>
$K$	<code>noverlap</code>
$M$	<code>n_seg</code>
$O$	<code>n_avg</code>
$f_s$	<code>fs</code>
$f_{\max}$	<code>f_max</code>
$f_{\min}$	<code>f_min</code>

4: Let's call her Alice.

5: `DAQSettings` inherits from the builtin `dict` and as such can contain arbitrary other keys besides those listed in Table 3.1. However, automatic validation of parameter consistency is only performed for these special keys.

6: Since the graph spanned by the parameters is not acyclic, this only works most of the time.

7: Settings are automatically parsed when passed to the `take()` method of the `Spectrometer` class.

**Listing 3.1:** `DAQSettings` example showcasing automatic parameter resolution. `n_avg` determines the number of outer averages, i.e., the number of data buffers acquired and processed individually.

```
{'f_min': 14.30511474609375,
 'f_max': 72000.0,
 'fs': 234375.0,
 'df': 14.30511474609375,
 'nperseg': 16384,
 'noverlap': 0,
 'n_seg': 1,
 'n_pts': 16384,
 'n_avg': 1}
```

**Listing 3.2:** Resolved settings for the same input parameters as in Listing 3.1 but for the `ZurichInstrumentsMFLIScope` backend with hardware constraints on `n_pts` and `fs`.

8: [https://docs.zhinst.com/labone\\_api\\_user\\_manual/modules/scope/index.html](https://docs.zhinst.com/labone_api_user_manual/modules/scope/index.html)

9: And issued a warning to inform the user their requested settings could not be matched.

ods. Their functionality is best illustrated by the internal workflow as representatively shown in Listing 3.3.

```

daq = MyDAQ(driver_handle)

parsed_settings = daq.setup(**user_settings)
acquisition_generator = daq.acquire(**parsed_settings)

for data_buffer in acquisition_generator:
    estimate_psd(data_buffer)

# Finalize, clean up, return to user code
...

```

When acquiring a new spectrum, all settings supplied by the user are first fed into the `setup()` method where instrument configuration takes place. The method returns the actual device settings,<sup>10</sup> which are then forwarded to the `acquire()` generator function. Here, the instrument is armed (if necessary), and subsequently data is fetched from the device and yielded to the caller `n_avg` times, where `n_avg` is the number of outer averages.<sup>11</sup> An exemplary implementation of a DAQ subclass for a fictitious instrument is shown in Listing 3.4. In addition to the methods to configure the instrument and perform data acquisition, it is possible to override the `DAQSettings` property to implement instrument-specific hardware constraints such as, in this example, the number of samples per buffer being constrained to the discrete interval `[1, 2048]`. Leveraging the `util.domains` module [33], more complex constraints such as sample rates restricted to an internal clock rate divided by a power of two<sup>12</sup> can be specified.

### 3.1.2 Data processing

Once time series data has been acquired using a given DAQ backend, it could in principle immediately be used to estimate the PSD following Equation 2.19. However, it is often desirable to transform, or process, the data in some fashion. This can include simple transformations such as accounting for the gain of a transimpedance amplifier (TIA) and convert the voltage back to a current,<sup>13</sup> or more complex ones such as applying calibrations. In particular, since the process of computing the PSD already involves Fourier transformation, the processing can also be performed in frequency space.

In `python_spectrometer`, this can be done using a `procfn` (in the time domain) or `fourier_procfn` (in the Fourier domain). The former is specified as an argument directly to the `Spectrometer` constructor. It is a callable with signature `(x, **kwargs) -> xp`, taking as arguments the time series data and arbitrary settings passed through from the `take()` method, and returns the processed data. Listing 3.5 shows a simple function that accounts for the gain of an amplifier. The latter is specified in the `psd_estimator` argument of the `Spectrometer` constructor. This argument allows the user to specify a custom estimator for the PSD, in which case a callable is expected. Otherwise, it should be a mapping containing parameters for the default PSD estimator, `scipy.signal.welch()` [32]. Here, the keyword `fourier_procfn` should be a callable with signature `(xf, f, **kwargs) -> (xfp, fp)`.<sup>14</sup> That is, it should

**Listing 3.3:** DAQ workflow pseudocode. A `MyDAQ` object (representing the instrument `My`) is instantiated with a driver object (for instance a `QCoDeS` Instrument). The instrument is configured with the given `user_settings`. Calling the generator function `daq.acquire()` with the actual device settings returns a generator, iterating over which yields one data buffer per iteration. The data buffers can then be passed to further processing functions (the PSD estimator in our example).

10: Which might differ from the requested settings as outlined above.

11: *I.e.*, the number of time series data batches acquired, as opposed to the number of Welch averages `n_seg` within one batch.

12: See for example the implementation of the [AlazarTech ATS9440](#) digitizer card.

13: Although it is of course less than trivial to discriminate between current and voltage noise in a TIA.

14: *I.e.*, the `psd_estimator` argument would be `{"fourier_procfn": fn}`.



```

# daq/mydaq.py
import dataclasses
from qutil.domains import DiscreteInterval
from .base import DAQ
from .settings import DAQSettings

@dataclasses.dataclass
class MyDAQ(DAQ):
    handle: mydriver.DeviceHandle

    @property
    def DAQSettings(self) -> type[DAQSettings]:
        class MyDAQSettings(DAQSettings):
            ALLOWED_NPERSEG = DiscreteInterval(1, 2048)
        return MyDAQSettings

    def setup(self, **settings) -> dict:
        settings = self.DAQSettings(settings)
        parsed_settings = settings.to_consistent_dict()
        self.handle.configure(parsed_settings)
        return parsed_settings

    def acquire(self, n_avg: int, *, **settings) -> Generator:
        self.handle.arm(n_avg)
        for _ in range(n_avg):
            self.handle.wait_for_trigger()
            yield self.handle.fetch()
        return self.handle.metadata

```

**Listing 3.4:** Exemplary code for a DAQ implementation of some instrument with given driver class `DeviceHandle` in the package `mydriver`. The `MyDAQ` class is instantiated with a `DeviceHandle` instance. Optionally, the `DAQSettings` property can be overridden to implement hardware constraints or default values for data acquisition parameters. For this, the `qutil.domains` module provides several classes that represent bounded domains and sets. The `setup()` method parses the given acquisition settings and configures the instrument through the external driver interface `handle.configure()`. The `acquire()` method arms the instrument (if necessary) and loops over the number of outer averages, `n_avg`. In the body of the loop, it can wait for external triggers (or send software triggers) before yielding a batch of data fetched from the external driver interface. Once acquisition is done, the method can return arbitrary metadata to the `Spectrometer` object to attach to the stored data.

take the frequency-space data, the corresponding frequencies, and arbitrary keyword arguments and return a tuple of the processed data and the corresponding frequencies.

A simple example for a processing function in Fourier space is shown in Listing 3.6, which computes the (anti-)derivative of the data using the fact that

$$\frac{\partial^n}{\partial t^n} \xrightarrow{\text{F.T.}} (i\omega)^n \quad (3.1)$$

under the Fourier transform. In ??, I discuss more complex use-cases of the processing functionality included in `python_spectrometer` in the context of vibration spectroscopy.

## 3.2 Feature overview

Now that we have a basic understanding of the design choices underlying `python_spectrometer`, let us discuss the typical workflow of using the package. Two modes of operation are to be distinguished: first, “serial” mode, in which users record new spectra manually, and second, “live” mode, in which new data is continuously being acquired. The former is well suited to a structured approach to noise spectroscopy where data is retained persistently and discrete changes are made to the system in between subsequent data acquisitions. The latter is aimed at a more fluent workflow in which data is not retained and data acquisition runs in the background.

### 3.2.1 Serial spectrum acquisition

The default mode for spectrum acquisition using `python_spectrometer` revolves around the `take()` method. Key to this workflow is the idea that each acquired spectrum be assigned a comment that allows to easily identify it in the main plot. For instance, this comment could contain information about the particular settings that were active when the spectrum was recorded, or where a particular cable was placed.

Consider as an example the procedure of “noise hunting”, *i.e.*, debugging a noisy experimental setup. The experimentalist,<sup>15</sup> having discovered that his data are noisier than expected, sets up the `Spectrometer` class with an instance of the `DAQ` subclass for the DAQ instrument connected to his sample, a Zurich Instruments MFLI.<sup>16</sup> Choosing to work with the demodulated data to benefit from the corresponding DAQ module’s larger flexibility, he recognizes that the resulting PSD will be the two-sided version because the data returned by the LIA is complex. Since he is interested in the physical frequencies<sup>17</sup> he sets the lock-in’s modulation frequency to 0 Hz and disables plotting the negative part of the frequency spectrum as it contains only redundant data in this case. Selecting the frequency bounds, say  $f_{\min} = 10$  Hz and  $f_{\max} = 100$  kHz, and using the sensible defaults for the remaining spectrum parameters, Bob first grounds the input of his DAQ to record a *baseline* spectrum. Thus far, his code would hence look something like that shown in Listing 3.7, which produces the plot shown in Figure 3.2.

The noise spectrum he obtains is white up until approximately 20 kHz where it starts falling off  $\propto f^{-n}$ . This is because the LIA low-pass filters the signal to suppress aliasing.<sup>18</sup> After acquiring the baseline, he next ungrounds the DAQ to obtain a representative spectrum of the noise in an actual measurement. He then proceeds by tweaking things on his

```
def comp_gain(x, gain=1.0, **_):
    return x / gain
```

**Listing 3.5:** A simple `procf`n, which converts amplified data back to the level before amplification. Note the token `**_` variable keyword argument that ensures no errors arise from other parameters being passed to the function. More complex processing chains can concisely be defined with `qutil.functools.FunctionChain` that pipes the output of one function into the input of the next.

```
def derivative(xf, f, n=0, **_):
    return xf / (2j * pi * f)**n
```

**Listing 3.6:** A simple `fourier_procf`n, which calculates the (anti-)derivative.

15: Let’s call him Bob.

16: For the MFLI, DAQ subclasses for both the `Scope` and the `DAQ` module are implemented. The former gives access to the signal before and the latter to the signal after demodulation.

17: A discussion of lock-in amplification is beyond the scope of this chapter. Here I will simply note that, for finite modulation frequencies  $f_m$ , LIAs will measure the PSD in the up-converted frequency band  $[-f_{\max} + f_m, f_m + f_{\max}]$  rather than the baseband.

18: Aliasing effects arise from finite sampling according to the Nyquist-Shannon sampling theorem [34–36]. It states that for a given physical bandwidth, the sampling rate  $f_s$  must be at least twice as large to faithfully reconstruct the signal in order to avoid aliasing, *i.e.*, the reverse of the argument we have made for the largest resolvable frequency  $f_{\max}$ . Some DAQ devices perform internal aliasing rejection while others do not.

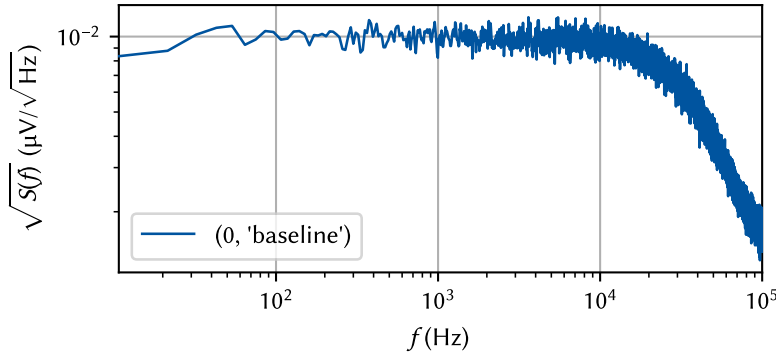
```

from python_spectrometer import Spectrometer, daq
from qutil.functools import scaled

mfli_daq = daq.ZurichInstrumentsMFLIDAQ(session, device)
spect = Spectrometer(mfli_daq, procfn=scaled(1e6),
                    plot_negative_frequencies=False,
                    processed_unit='μV')

settings = {'f_min': 1e1, 'f_max': 1e5, 'freq': 0}
spect.take('baseline', daq='grounded', **settings)

```



**Listing 3.7:** Setup and serial workflow using the python\_spectrometer package. session and device are application programming interface (API) objects of the zhinst.toolkit driver package. It is therefore possible to simply use the driver objects that are already in use in the measurement setup. The procfn and processed\_unit arguments help converting raw data into a more human-friendly unit.

**Figure 3.2:** The python\_spectrometer plot after acquiring the (here: synthetic) baseline spectrum. By default, the amplitude spectral density (ASD) =  $\sqrt{\text{PSD}}$  is displayed in the main plot. Each spectrum is assigned a unique identifier key consisting of an incrementing integer and the user comment, and can be referred to by either (or both) when interacting with the object.

setup, testing out different parameters, *etc.* Every time he changes something, he acquires another spectrum using `take()`, labeling each with a meaningful comment for identification. The code shown in Listing 3.8 would then leave him with the spectrometer plot as shown in Figure 3.3. While working, Bob realizes he'd like see the signal in the time domain as well. He easily achieves this by setting `spect.plot_timetrace = True`, which adds an oscilloscope subplot to the spectrometer figure as shown in Figure 3.4. Since his DAQ returns complex data, the absolute value  $R = X + iY$  is plotted.

```

settings['daq'] = 'connected'
spect.take('connected', **settings)
spect.take('lifted cable', cable='lifted', **settings)
spect.take('jumped', **settings)

```

**Listing 3.8:** Code to acquire additional spectra. Arbitrary key-value pairs can be passed to the `take()` method, which are stored as metadata if they do not apply to any functions downstream in the data processing chain.

Bob now observes that the noise spectra he has recorded display many sharp peaks in particular at high frequencies while the  $1/f$  noise floor seems pretty consistent across different measurements. This makes it harder for him to evaluate whether any of his changes are actually an improvement or not. The python\_spectrometer package allows addressing this by plotting the integrated spectra in another subplot. Bob's spectrometer figure after setting `spect.plot_cumulative = True` is shown in Figure 3.5. In the case that `spect.plot_amplitude == True`, this new subplot shows the RMS in the band  $[f_{\min}, f]$ ,

$$\text{RMS}_S(f) \equiv \text{RMS}_S(f_{\min}, f), \quad (3.2)$$

and the band power (Equation 2.14) otherwise.

The cumulative RMS plot already helps, but Bob would like a more quantitative comparison of relative spectral powers. Therefore, he rescales the spectra in terms of their relative powers expressed in dB<sup>19</sup> by applying the following settings, which changes the plot to the layout shown

19: Recall that the decibel is defined by the ratio  $L_p$  of two powers  $P_1, P_2$  as [37]

$$L_p = 10 \log_{10} \left( \frac{P_1}{P_2} \right) \text{ dB}.$$

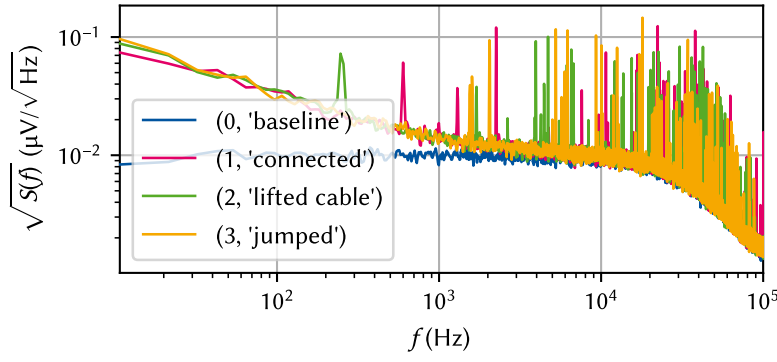


**Figure 3.3:** The `python_spectrometer` plot after acquiring additional (synthetic) spectra. Each spectrum is uniquely identified by a two-tuple of (index, comment).

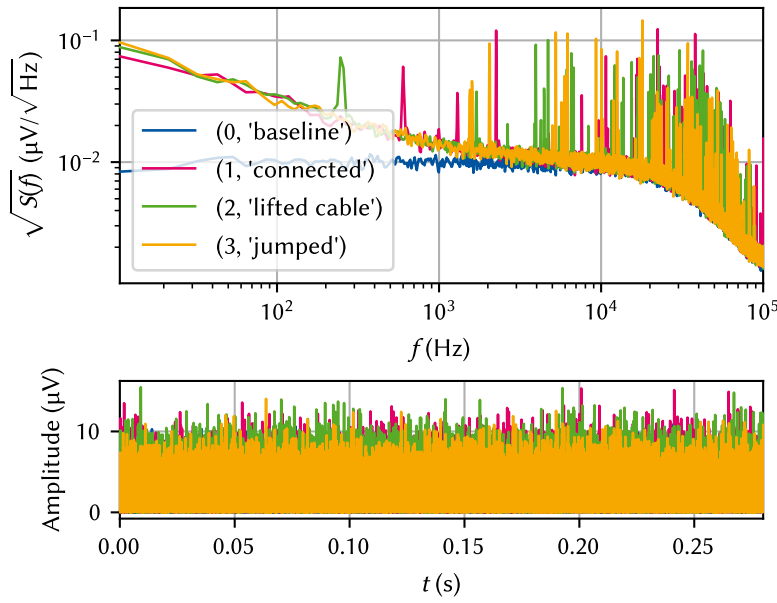


**Figure 3.4:** The `python_spectrometer` plot shown in Figure 3.3 when setting `spect.plot_timetrace = True`. This adds a subplot that shows the time series data from which the PSD was computed akin to what an oscilloscope would show. For complex time series, the absolute value  $R = X + iY$  is plotted. Note that this is the entire time series, *i.e.*, the data of length  $L$ , which is (by default, using Welch's method) segmented for spectrum estimation.

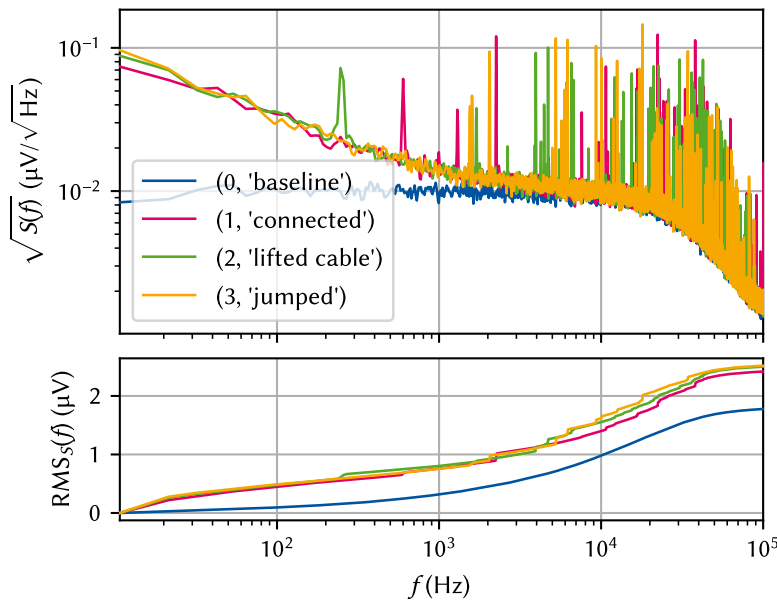


**Figure 3.5:** The `python_spectrometer` plot shown in Figure 3.3 when setting `spect.plot_cumulative = True`. This adds a subplot that shows the RMS (see Equation 2.14) which can be helpful in evaluating the contribution of individual peaks in the spectrum to the total noise power. Both the oscilloscope subplot (Figure 3.4) and the RMS subplot can also be shown at the same time.

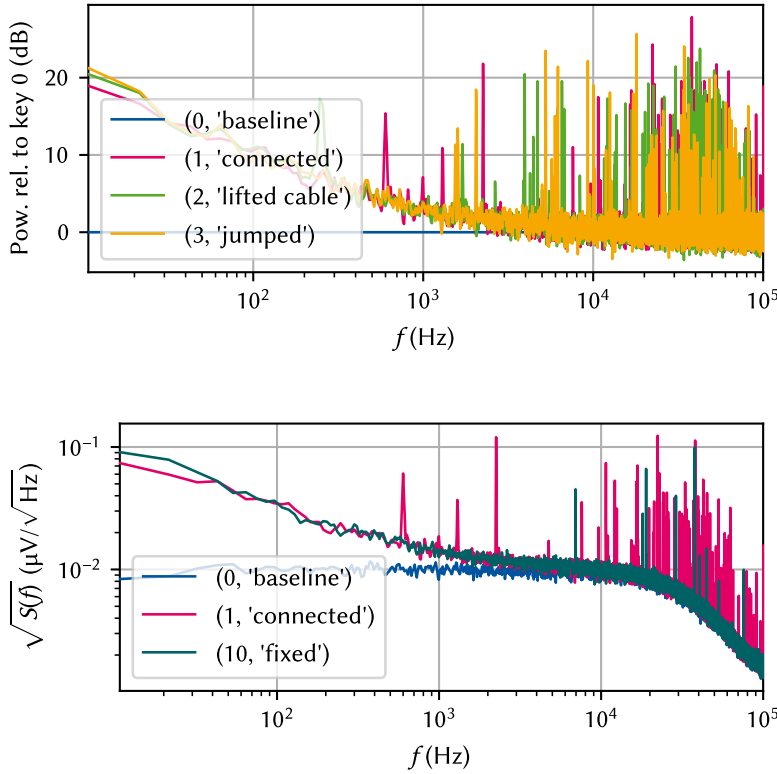


**Figure 3.6:** The `python_spectrometer` plot in relative mode. Starting from the state in Figure 3.3, we set `spect.plot_dB_scale = True` as well as `spect.plot_amplitude = False` and `spect.plot_density = False` to compare the relative noise powers with respect to the baseline.

**Figure 3.7:** The `python_spectrometer` plot after multiple additional spectra were acquired and hidden. Hiding spectra that one is not interested in anymore is achieved through `spect.hide(*range(2, 10))`. This is reversed by `spect.show(*range(2, 10))`. Data can also be dropped (`spect.drop(key)`) or deleted (`spect.delete(key)`) from the internal cache and disk, respectively.

in Figure 3.6:

```
| spect.plot_dB_scale = True
| spect.plot_amplitude = False
| spect.plot_density = False
```

The attribute `plot_density` controls whether the *power spectral density* or the *power spectrum* is plotted.<sup>20</sup> Scaling the data to the power spectrum instead of the density, Bob can get an estimate of the RMS at a single frequency by reading off the peak height. Additionally displaying the data in dB then gives insight into relative noise powers of different spectra.

Bob carries on with his enterprise and continues to acquire spectra until, finally, he finds the source of his noise! Alas, his spectrometer plot is now overflowing with plotted data when really he just wants to compare the baseline, the original, noisy state, and the final, clean spectrum. He simply calls

```
| spect.hide(*range(2, 10))
```

to hide the eight spectra of unsuccessful debugging, leaving him with a plot as shown in Figure 3.7.

Finally, happy with the results, Bob serializes the state of the spectrometer to disk, allowing him to pick up where he left off at a later point in time:

```
| spect.serialize_to_disk('2032-12-24_noise_hunting')
```

The next week, Bob is asked by his team about his progress on debugging the noise in their setup. Even though he is working from home that day and does not have access to the lab computer, Bob simply uses his laptop

20: At this point, we *do* need to distinguish between the PSD and the power spectrum counter to Sidenote 10 in Chapter 2. The PSD and power spectrum are related by the equivalent noise bandwidth (ENBW),

$$\text{Spectral density} \xrightarrow{\times \text{ENBW}} \text{Spectrum},$$

which is itself a function of the sampling rate and the properties of the spectral window [21],

$$\text{ENBW} = f_s \frac{\sum_n \hat{w}_n^2}{\left[\sum_n \hat{w}_n\right]^2}. \quad (3.3)$$

computer and pulls up the Spectrometer session stored on the server, allowing them to interactively discuss the spectra:

```
| file = '2032-12-24_noise_hunting'
| # Read-only instance because no DAQ attached
| spect = Spectrometer.recall_from_disk(savepath / file)
```

This opens up the plot shown in Figure 3.7 again. While they cannot acquire new spectra in this state,<sup>21</sup> they can still use all the plotting features like showing or hiding spectra, or changing plot types as discussed above.

21: They could of course always attach a DAQ instance to the spectrometer and continue as they were.

### 3.2.2 Live spectrum acquisition

Manually recording spectra in the workflow outlined in Subsection 3.2.1 becomes tedious at some point, and experimenters tend to become negligent with keeping metadata and comments up to date as they continue to change settings. Once a certain number of spectra has been obtained, the spectrometer plot also becomes crowded, and hiding old spectra manually is cumbersome. Moreover, each time a spectrum is captured, data is saved to disk, potentially accruing large amounts of storage space. For these reasons, the python\_spectrometer package also offers a non-persistent live mode for displaying spectra continuously.

This mode is facilitated by the `util.plotting.live_view` module that provides asynchronous plotting functionality based on `matplotlib`. The `live_view` module supports both the multithreading and multiprocessing paradigms for concurrency in order to keep the interpreter responsive.<sup>22</sup> In the former case, the window hosting the figure runs in the main thread and is kept responsive using `matplotlib`'s graphical user interface (GUI) event loop mechanisms. In the latter, the plotting takes place in a separate process, resulting in true parallelism.

22: Note that technically, data is also recorded in a background thread in serial mode by default.

The live mode is started with the `Spectrometer.live_view()` method. Data is continuously acquired in a background thread using the same DAQ interface as the serial mode. Instead of saving the data on disk and managing plotting from `python_spectrometer`, however, the data is fed into a queue.<sup>23</sup> A `live_view.IncrementalLiveView2D` object then retrieves the data from the queue and handles plotting in the GUI event loop. To start a spectroscopy session with the same parameters as in Subsection 3.2.1 with a given `Spectrometer` object (see Listing 3.7), we would call

```
| view = spect.live_view(f_min=1e1, f_max=1e5, in_process=True)
```

23: A queue is a concurrency mechanism for exchanging data between multiple threads or processes.

which would open a figure window such as that shown in Figure 3.8. Similar to `take()`, the data acquisition parameters are passed to `live_view()` as keyword arguments.<sup>24</sup> The `in_process` argument specifies if multiprocessing (`True`) or multithreading (`False`) is used. Dictionaries with customization parameters for the `live_view` object can further be passed to the method. Functionality to take snapshots to retain live data is currently not implemented but would be a valuable addition to the noise-hunting workflow.

24: The difference is, of course, that we do not need to specify a comment since no data is retained.

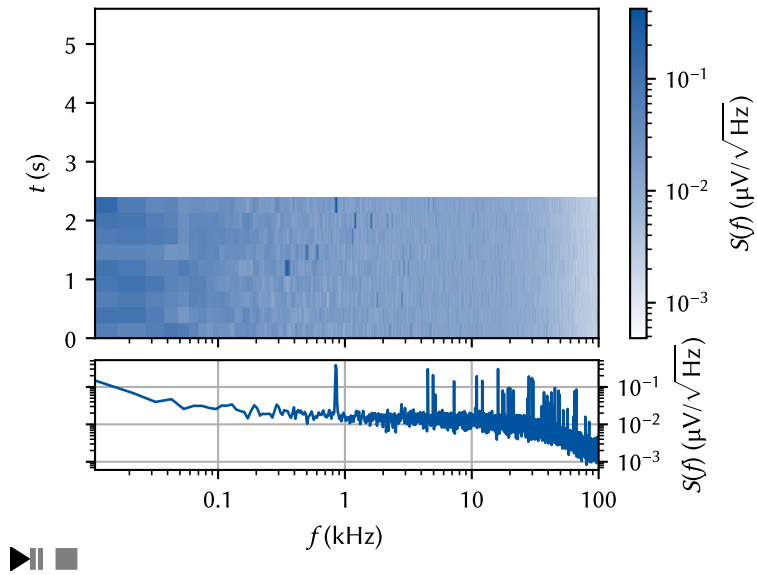


**Figure 3.8:** Spectrometer live view. The bottom plot shows the most recently acquired spectrum, while the top plot shows a waterfall plot of the most recent ones. Data acquisition runs in a background thread, keeping the interpreter responsive and available to interact with instruments, for example. The icons in the bottom left and right corners allow interacting with the live view.



# Conclusion and outlook

# 4

**I**n this part of the present thesis, I introduced the `python_spectrometer` Python package for interactive, backend-agnostic noise spectroscopy. I first presented the theory behind spectral noise estimation based on time series analysis in Chapter 2. There, I showed how, by the Wiener-Khinchin theorem, the PSD  $S(\omega)$  is related to a time-dependent signal by the Fourier transform of its autocorrelation function  $C(\tau)$ . After discretizing the problem, I discussed how the arising spectral windowing introduces distortions in the estimated PSD through effects such as spectral leakage and scalloping loss. The introduction of windowing naturally led to the need for a more efficient method of spectrum estimation to avoid data wastefulness. This is addressed by Welch’s method, which trades spectral resolution for estimation accuracy for a given input size by dividing the input into segments and letting them overlap. Finally, I discussed the various parameters that influence the properties of the spectrum estimate produced by Welch’s method.

In Chapter 3, I then introduced the `python_spectrometer` package that facilitates noise spectroscopy based on the theory developed in the previous chapter. While in principle agnostic to the specific technique (simple periodogram, Bartlett’s method, *etc.*), it employs Welch’s method by default to perform efficient estimation of noise power spectral densities. To make noise spectroscopy as approachable as possible, the package provides a unified interface to various hardware and software backends to manage data acquisition. Furthermore, it incorporates rich plotting features to ease data analysis and thereby expedite the feedback loop with the lab. I first outlined the design choices underlying the source code and explained the mechanism employed to infer DAQ settings from, for example, the physical parameters of the resulting spectrum estimate. I described the interface to drivers for different hardware instruments that makes it possible to use the same user code for spectrum acquisition independent of the specific instrument used for data acquisition while at the same time keeping the amount of required driver code at a minimum. Finally, I showcased the interactive features by means of a typical workflow. Here, the serial approach of recording single spectra that are saved to disk at a time stands in contrast to the non-persistent live mode, where data is continuously acquired and displayed in a separate thread or process.

There are several possible avenues for future development of the `python_spectrometer` package. An obvious case is adding support for more DAQ hardware instruments by implementing DAQ interfaces. Modular devices such as those offered by QBLOX<sup>1</sup> and Quantum Machines<sup>2</sup> are on track to become the new standard in quantum technology labs. Implementing drivers for these instruments would benefit the adoption of both the instruments and the `python_spectrometer` package. Another valuable addition would be supporting generic instruments abstracted by QuMADA [38]. QuMADA is a QCoDeS-based measurement framework that provides a unified interface to instruments in order to – in a similar spirit to `python_spectrometer`’s DAQ interface – abstract away internals of individual instruments and provide users with a standardized way to interact with them. This approach should naturally lend itself to a single implementation of the DAQ class supporting various instruments through the unified QuMADA interface.

1: <https://www.qblox.com/research>

2: <https://www.quantum-machines.co/>



Next, incorporating noise spectroscopy into the standard measurement workflow of quantum device experiments would allow experimentalists to quickly gauge noise levels as they are performing measurements. If for some reason the noise changed<sup>3</sup> the experimentalist could quickly obtain insight into the noise by analyzing the spectrum. In a client-server architecture, which is inherently asynchronous, such as Zurich Instrument's LabOne<sup>4</sup> software, this is already possible using the web interface. But of course the strength of the `python_spectrometer` package stems from its capacity to be utilized in conjunction with any hardware instrument.

One way to implement such functionality would be to introduce a proxy DAQ subclass to be used together with the live mode presented in Subsection 3.2.2. This proxy class would serve as an interface to external measurement software and expose two attributes; first, a data queue, into which the external code could place arbitrary time series data that was obtained during some measurement, and second, a shared dictionary to hold acquisition parameters as these might change between measurements. Because the live view mode runs in the background, the external measurement framework could push data to the queue whenever new data was taken without obstructing the measurement workflow.

Listing 4.1 shows a template design for such a TeeDAQ class.<sup>5</sup> The `setup()` method ignores the input parameters and instead obtains the current settings from the shared settings proxy. Similarly, instead of fetching data from an instrument itself, the `acquire()` method attempts to fetch data from the shared queue and blocks the thread if no data is present, thereby efficiently idling and consuming no resources unless triggered by the external caller. A measurement framework would then interact with the TeeDAQ object as exemplarized by the following code:

```
daq = TeeDAQ(...)
spect = Spectrometer(daq)
view = spect.live_view()
...
data = measure(fs, n_pts)
daq.settings.update(fs=fs, n_pts=n_pts)
daq.queue.put(data)
```

Measurement frameworks integrating with this interface could thus provide experimentalists live feedback on current noise levels with negligible overhead and minimal code adaptation.

Finally, it might be useful to not only allow estimating PSDs but also cross power spectral densities (CSDs) or *cross-spectra*. The cross-spectrum<sup>6</sup> is the Fourier transform of not the autocorrelation but the cross-correlation function  $C(\tau)$  (Equation 2.4) between two random processes. Take a set of processes  $\{x_1(t), x_2(t), \dots, x_n(t)\}$  that correspond to noise measured at different locations in a sample. The cross-correlation function between variables  $x_i$  and  $x_j$  is then given by<sup>7</sup>

$$C_{ij}(\tau) = \langle x_i(t)^* x_j(t + \tau) \rangle. \quad (4.1)$$

This function (and its Fourier pair the cross-spectrum  $S_{ij}(\omega)$ ) quantifies the degree of correlation between noise at site  $i$  and noise at site  $j$ . Unlike the *auto*-spectrum (or self-spectrum), the cross-spectrum is always a complex quantity, even for real  $x_i(t)$ . It is not hard to see that for quantum processors, for example, these kinds of correlations could have significant impact on operation, and on error correction in particular [39–41]. To incorporate cross-spectra in the `python_spectrometer` package, only small changes should be necessary.

3: As it happens often, unfortunately.

4: <https://www.zhinst.com/ch/en/instruments/labone/labone-instrument-control-software>

```
# daq/tee.py
import dataclasses
import threading
import multiprocessing as mp

from .base import DAQ

@dataclasses.dataclass
class TeeDAQ(DAQ):
    settings:
        ↪ mp.managers.DictProxy
    queue: mp.JoinableQueue
    event: threading.Event

    def setup(self, **_):
        settings = self.
        ↪ DAQSettings(self.
        ↪ settings)
        return settings.
        ↪ to_consistent_dict()

    def acquire(self, **_):
        while not
        ↪ self.event.is_set():
            yield self.queue.
            ↪ get(block=True)
```

**Listing 4.1:** Template design for a proxy DAQ implementation to stream noise spectra from an external measurement framework. The `settings` attribute is a dictionary proxy shared between processes and used to pass acquisition parameters from the measurement framework to `python_spectrometer`.

5: The UNIX shell command `data = $(measure(**settings) | tee daq)` should give an indication as to the naming.

6: Again, we use the two terms interchangeably unless otherwise indicated, see Sidenote 10 in Chapter 2.

7: Again assuming wide-sense stationary processes.

First, the data acquisition logic would need to be adapted. Two possible routes suggest themselves here; first, specialized DAQ classes could be implemented that, in place of yielding one batch of time series data, yield two batches each time they are queried. This approach first of all requires instruments with multiple channels,<sup>8</sup> which is not necessarily given. Furthermore, it would incur additional coding efforts by having to re-implement each DAQ class for cross-spectra. On the other hand, it would arguably make synchronization between channels easier to achieve.

A less involved path would adapt the Spectrometer class to work with multiple DAQs. This would not involve additional driver work<sup>9</sup> and allow the Spectrometer object to ensure synchronization between the different DAQs. The internal workflow shown in Listing 3.3 would then need to be slightly adapted to the code shown in Listing 4.2. The downside of this approach is that synchronization of different instruments or channels would need to be taken care of externally.

```
daq_1 = MyDAQ(driver_handle, channel=1)
# Or MyOtherDAQ(driver_handle_2) if another instrument
daq_2 = MyDAQ(driver_handle, channel=2)
daqs = (daq_1, daq_2)

parsed_settings = [daq.setup(**user_settings) for daq in daqs]
assert all_equal(parsed_settings), "DAQ settings do not match"

acquisition_generators = [daq.acquire(**parsed_settings[0])
                           for daq in daqs]
for data_buffers in zip(*acquisition_generators):
    estimate_csd(*data_buffers)
```

Further code adaptations would involve minor changes such as replacing the spectrum estimator with `scipy.signal.csd()` [42] for CSD estimation<sup>10</sup> and making the plotting conform to complex data.<sup>11</sup>

8: If one sticks to single DAQ instances managing single instruments.

9: Except possibly ensuring thread safety and timing synchronization if multiple DAQ objects communicate with the same physical instrument.

**Listing 4.2:** Proposed DAQ workflow for estimating cross-spectra. Each hardware channel (same or different instruments) is assigned to a DAQ object. After instrument configuration, it is asserted that the parameters match. Finally, data is fetched from both channels and fed into a CSD estimator. Note that triggering would need to be implemented externally.

10: In practice, working with the normalized CSD, or correlation coefficient [43, 44]

$$r_{ij}(\omega) = \frac{S_{ij}(\omega)}{\sqrt{S_{ii}(\omega)S_{jj}(\omega)}} \quad (4.2)$$

with  $S_{ii}(\omega)$  the PSD of process  $x_i$  would likely be more favorable.

11: It could be worthwhile to add a subplot to display both the magnitude and phase of the complex quantity  $S_{ij}(\omega)$ .

## **Part II**

# **CHARACTERIZATION AND IMPROVEMENTS OF A MILLIKELVIN CONFOCAL MICROSCOPE**

**Part III**

**OPTICAL MEASUREMENTS OF  
ELECTROSTATIC EXCITON TRAPS IN  
SEMICONDUCTOR MEMBRANES**

## **Part IV**

# **A FILTER-FUNCTION FORMALISM FOR UNITAL QUANTUM OPERATIONS**

# **APPENDIX**

# Supplementary to Part IV: Filter-function derivations and validation



In this appendix, we give additional information on the filter-function formalism presented in Part IV. We first show additional derivations that were omitted from the main text in Section A.1, and derive bounds on the Magnus expansion (ME) convergence in Section A.2. In Section A.3, we augment the filter function (FF) formalism of the main text by deriving a concatenation rule for the second-order terms of the ME. This enables a more efficient calculation of the full quantum process including coherent errors for sequences of quantum gates together with the rule for first-order terms given in Subsection 6.2.1. In Section A.4, we review time-domain simulation methods of noisy quantum dynamics, which we employ in Section A.5 to validate our FF formalism's predicted fidelities for the quantum gates of Reference 45 and discussed in Section 9.1, as well as the quantum Fourier transform (QFT) algorithm presented in Section 9.4. We use the notation set in Section 6.1 except where indicated otherwise.

<b>A.1</b>	<b>Additional derivations</b>	76
<b>A.2</b>	<b>Convergence Bounds</b>	79
<b>A.3</b>	<b>Concatenation of second-order filter functions</b>	81
<b>A.4</b>	<b>Monte Carlo and GKSL master equation simulations</b>	85
<b>A.5</b>	<b>Fidelity validation</b>	87

## A.1 Additional derivations

### A.1.1 Derivation of the single-qubit cumulant function in the Liouville representation

For a single qubit, the Pauli basis  $\mathcal{P}_1 = \{\sigma_i\}_{i=0}^3 = 1/\sqrt{2} \times \{\mathbb{1}, \sigma_x, \sigma_y, \sigma_z\}$  is a natural choice to define the Liouville representation. In this case, the trace tensor Equation 6.18 can be simplified and thus Equation 6.17 given a more intuitive form which we derive in this subsection. Since the cumulant function is linear in the noise indices  $\alpha, \beta$  we drop them in the following for legibility. Our results hold for both a single pair of noise indices and the total cumulant. We start by observing the relation

$$T_{klij} = \text{tr}(\sigma_k \sigma_l \sigma_i \sigma_j) = \frac{1}{2}(\delta_{kl}\delta_{ij} - \delta_{ki}\delta_{lj} + \delta_{kj}\delta_{li}) \quad (\text{A.1})$$

for the Pauli basis elements  $\sigma_k, k \in \{1, 2, 3\}$ . Including the identity element  $\sigma_0$  in the trace tensor gives additional terms. However, as we show now none of these contribute to  $\mathcal{K}$  because they cancel out.

First, since the noise Hamiltonian  $H_n(t)$  is traceless and therefore  $\tilde{\mathcal{B}}_{\alpha 0}(t) = 0$ , we have  $\Gamma_{kl}, \Delta_{kl} \propto (1 - \delta_{k0})(1 - \delta_{l0})$ , i.e. the first column and row of both the decay amplitude and frequency shift matrices are zero, and hence terms in the sum of Equation 6.17 with either  $k = 0$  or  $l = 0$  vanish. Next, for  $i = j = 0$  all of the traces cancel out as can be easily seen. The last possible cases are given by  $i = 0, j \neq 0$  and vice versa. For these cases we have

$$T_{kl0j} = T_{klj0} = \frac{1}{\sqrt{2}} \text{tr}(\sigma_k \sigma_l \sigma_j) = \frac{i}{2} \varepsilon_{klj} \quad (\text{A.2})$$

with  $\varepsilon_{klj}$  the completely antisymmetric tensor. Both of the above cases vanish in  $\mathcal{K}$  since, taking the case  $j = 0$  for example,

$$\frac{1}{2} (T_{kl0i} - T_{k0li} - T_{ki0l} + T_{kiol}) = \frac{i}{2} (\varepsilon_{kli} - \varepsilon_{kli} - \varepsilon_{kil} + \varepsilon_{kil}) = 0 \quad (\text{A.3a})$$

for the decay amplitudes  $\Gamma$  and

$$\frac{1}{2} (T_{kl0i} - T_{lk0i} - T_{kli0} + T_{lki0}) = \frac{i}{2} (\varepsilon_{kli} - \varepsilon_{lki} - \varepsilon_{kli} + \varepsilon_{lki}) = 0 \quad (\text{A.3b})$$

for the frequency shifts  $\Delta$ . Hence, only terms with  $i, j > 0$  contribute and we can plug the simplified expressions for the trace tensor  $T_{klj}$ , Equation A.1, into Equation 6.17 to write the cumulant function for a single qubit and the Pauli basis concisely as

$$\mathcal{K}_{ij}(\tau) = -\frac{1}{2} \sum_{kl} \left[ \Delta_{kl} (T_{klji} - T_{lkji} - T_{klij} + T_{lkij}) \right. \quad (\text{A.4})$$

$$\left. + \Gamma_{kl} (T_{klji} - T_{kjli} - T_{kilj} + T_{kijl}) \right] \\ = - \sum_{kl} \left[ \Delta_{kl} (\delta_{ki} \delta_{lj} - \delta_{kj} \delta_{li}) + \Gamma_{kl} (\delta_{kl} \delta_{ij} - \delta_{kj} \delta_{li}) \right] \quad (\text{A.5})$$

$$= \Delta_{ji} - \Delta_{ij} + \Gamma_{ij} - \delta_{ij} \text{tr } \Gamma \quad (\text{A.6})$$

$$= \begin{cases} - \sum_{k \neq i} \Gamma_{kk} & \text{if } i = j, \\ -\Delta_{ij} + \Delta_{ji} + \Gamma_{ij} & \text{if } i \neq j, \end{cases} \quad (\text{A.7})$$

as given in the main text.

### A.1.2 Evaluation of the integrals in Equation 6.40

Here we calculate the integrals appearing in the calculation of the frequency shifts  $\Delta$ , Equation 6.41, given by

$$I_{ijmn}^{(g)}(\omega) = \int_{t_{g-1}}^{t_g} dt e^{i\Omega_{ij}^{(g)}(t-t_{g-1})-i\omega t} \int_{t_{g-1}}^t dt' e^{i\Omega_{mn}^{(g)}(t'-t_{g-1})+i\omega t'}. \quad (\text{A.8})$$

The inner integration is simple to perform and we get

$$I_{ijmn}^{(g)}(\omega) = \int_{t_{g-1}}^{t_g} dt e^{i\Omega_{ij}^{(g)}(t-t_{g-1})-i\omega(t-t_{g-1})} \\ \times \begin{cases} \frac{e^{i(\omega+\Omega_{mn}^{(g)})(t-t_{g-1})} - 1}{i(\omega + \Omega_{mn}^{(g)})} & \text{if } \omega + \Omega_{mn}^{(g)} \neq 0 \\ t - t_{g-1} & \text{if } \omega + \Omega_{mn}^{(g)} = 0. \end{cases} \quad (\text{A.9})$$

Shifting the limits of integration and performing integration by parts in the case  $\omega + \Omega_{mn}^{(g)} = 0$  then yields

$$I_{ijmn}^{(g)}(\omega) = \begin{cases} \frac{1}{\omega + \Omega_{mn}^{(g)}} \left( \frac{e^{i(\Omega_{ij}^{(g)} - \omega)\Delta t_g} - 1}{\Omega_{ij}^{(g)} - \omega} - \frac{e^{i(\Omega_{ij}^{(g)} + \Omega_{mn}^{(g)})\Delta t_g} - 1}{\Omega_{ij}^{(g)} + \Omega_{mn}^{(g)}} \right) & \text{if } \omega + \Omega_{mn}^{(g)} \neq 0, \\ \frac{1}{\Omega_{ij}^{(g)} - \omega} \left( \frac{e^{i(\Omega_{ij}^{(g)} - \omega)\Delta t_g} - 1}{\Omega_{ij}^{(g)} - \omega} - i\Delta t_g e^{i(\Omega_{ij}^{(g)} - \omega)\Delta t_g} \right) & \text{if } \omega + \Omega_{mn}^{(g)} = 0 \wedge \Omega_{ij}^{(g)} - \omega \neq 0, \\ \frac{\Delta t_g^2}{2} & \text{if } \omega + \Omega_{mn}^{(g)} = 0 \wedge \Omega_{ij}^{(g)} - \omega = 0. \end{cases} \quad (\text{A.10})$$



### A.1.3 Simplifying the calculation of the entanglement infidelity

In the main text, we claimed that the contribution of noise sources  $(\alpha, \beta)$  to the total entanglement infidelity  $I_{\text{ent}}(\tilde{\mathcal{U}}) = \sum_{\alpha\beta} I_{\alpha\beta}$  reduces from the trace of the cumulant function  $\mathcal{K}$  to

$$I_{\alpha\beta} = -\frac{1}{d^2} \text{tr } \mathcal{K}_{\alpha\beta} \quad (\text{A.11})$$

$$= \frac{1}{d} \text{tr } \Gamma_{\alpha\beta}. \quad (\text{A.12})$$

To show this, we substitute  $\mathcal{K}$  by its definition in terms of  $\Delta$  and  $\Gamma$  according to Equation 6.17. This yields for the trace

$$\begin{aligned} \text{tr } \mathcal{K}_{\alpha\beta} &= -\frac{1}{2} \sum_{kl} \delta_{ij} (f_{ijkl} \Delta_{\alpha\beta,kl} + g_{ijkl} \Gamma_{\alpha\beta,kl}) \\ &= -\frac{1}{2} \sum_{ikl} \Gamma_{\alpha\beta,kl} (T_{kl\bar{i}\bar{i}} + T_{lk\bar{i}\bar{i}} - 2T_{k\bar{i}\bar{i}l}) \end{aligned} \quad (\text{A.13})$$

since  $\Delta$  is antisymmetric. In order to further simplify the trace tensors on the right hand side of Equation A.13, we observe that the orthonormality and completeness of the operator basis  $\mathbf{C}$  defining the Liouville representation of  $\mathcal{K}$  (cf. Equation 6.14) is equivalent to requiring that  $\mathbf{C}^\dagger \mathbf{C} = \mathbb{1}$  with  $\mathbf{C}$  reshaped into a  $d^2 \times d^2$  matrix by a suitable mapping. This condition may also be written as

$$\begin{aligned} \delta_{ac} \delta_{bd} &= \sum_k C_{k,ab}^* C_{k,cd} \\ &= \sum_k C_{k,ba} C_{k,cd} \end{aligned} \quad (\text{A.14})$$

because every element  $C_k$  is Hermitian. Using this relation in Equation A.13 then yields

$$\begin{aligned} \text{tr } \mathcal{K}_{\alpha\beta} &= -\frac{1}{2} \sum_{kl} \Gamma_{\alpha\beta,kl} (2d\delta_{kl} - 2\text{tr}(C_k)\text{tr}(C_l)) \\ &= -d \text{tr } \Gamma_{\alpha\beta}. \end{aligned} \quad (\text{A.15})$$

The last equality only holds true for bases with a single non-traceless element (the identity), such as the bases discussed in Section 6.8. This is because in this case,  $\text{tr}(C_k) = 0$  for  $k > 0$  whereas  $\Gamma_{\alpha\beta,kl} = 0$  for either  $k = 0$  or  $l = 0$  since  $\Gamma$  is a function of the traceless noise Hamiltonian for which  $\text{tr}(C_0 H_n) \propto \text{tr } H_n = 0$  (i.e. the first column of the control matrix is zero, see Equations 6.16 and 6.21). Finally, substituting Equation A.15 into Equation A.11 we obtain our result

$$I_{\alpha\beta} = \frac{1}{d} \text{tr } \Gamma_{\alpha\beta}. \quad (\text{A.16})$$

### A.1.4 Sum rule

For white noise, the infidelity to leading order does not depend on the internal dynamics of the control operation but only on the total duration  $\tau$ . To see this, take Equation 6.21 and substitute the correlation function of white noise,  $\langle b_\alpha(t_1) b_\alpha(t_2) \rangle = S_0 \delta(t_1 - t_2)$ . The integrals then simplify

to

$$\Gamma_{\alpha\alpha,kl} = S_0 \int_0^\tau dt \tilde{\mathcal{B}}_{\alpha k}(t) \tilde{\mathcal{B}}_{\alpha l}(t). \quad (\text{A.17})$$

In order to compute the infidelity, we require the trace over the matrix of decay amplitudes (Equation 6.48), so

$$I_\alpha = \frac{S_0}{d} \text{tr} \Gamma_{\alpha\alpha} = \frac{1}{d} \sum_k \int_0^\tau dt \tilde{\mathcal{B}}_{\alpha k}^2(t). \quad (\text{A.18})$$

Now recall that  $\tilde{\mathcal{B}}$  is a vector on Liouville space and we can write  $\tilde{\mathcal{B}}_\alpha(t) \doteq |\tilde{B}_\alpha(t)\rangle\rangle \equiv \langle\langle \tilde{B}_\alpha(t) |$  because it is Hermitian. Thus,

$$I_\alpha = \frac{S_0}{d} \int_0^\tau dt \langle\langle \tilde{B}_\alpha(t) | \tilde{B}_\alpha(t) \rangle\rangle = \frac{1}{d} \int_0^\tau dt \|\tilde{B}_\alpha(t)\|^2, \quad (\text{A.19})$$

and if  $B_\alpha(t) = B_\alpha$ , i. e., is time-independent, the integral evaluates simply to  $\tau$ ,

$$I_\alpha = \frac{S_0 \tau}{d} \|\tilde{B}_\alpha\|^2, \quad (\text{A.20})$$

because the control unitary  $U_c(t)$  conserves the norm. Since also  $I_\alpha = \int d\omega / 2\pi d S(\omega) \mathcal{F}_\alpha(\omega)$  with the fidelity filter function  $\mathcal{F}_\alpha(\omega)$  (Equations 6.26 and 6.49), this result also implies the sum rule

$$\int \frac{d\omega}{2\pi} \mathcal{F}_\alpha(\omega) = \tau \|\tilde{B}_\alpha\|^2, \quad (\text{A.21})$$

a result previously obtained by Cywiński et al. [46]. This means that pulse shaping and similar techniques never yield a leading-order fidelity enhancement if the noise is white in the relevant regime of frequencies as the fidelity only depends on the total duration of the pulse.

## A.2 Convergence Bounds

In this section we give bounds for the convergence of the expansions employed in the main text for the case of purely autocorrelated noise,  $S_{\alpha\beta}(\omega) = \delta_{\alpha\beta} S_\alpha(\omega) = S_\alpha(\omega)$ , following the approach by Green et al. [47]. For Gaussian noise, our expansion is exact when including first and second order Magnus expansion (ME) terms. Hence, the convergence radius of the ME becomes infinite and the fidelity can be computed exactly by evaluating the matrix exponential Equation 6.11. For non-Gaussian noise, the following considerations apply.

### A.2.1 Magnus Expansion

The ME of the error propagator Equation 6.8a converges if  $\int_0^\tau dt \|\tilde{H}_n(t)\| < \pi$  with  $\|A\|^2 = \langle A, A \rangle = \sum_{ij} |A_{ij}|^2$  the Frobenius norm [48]. We assume a time dependence of the noise operators of the form  $B_\alpha(t) = s_\alpha(t) B_\alpha$ . By

the Cauchy-Schwarz inequality we then have

$$\begin{aligned}
 \|\tilde{H}_n(t)\|^2 &= \|H_n(t)\|^2 \\
 &= \sum_{\alpha\beta} s_\alpha(t)s_\beta(t)b_\alpha(t)b_\beta(t)\langle B_\alpha, B_\beta \rangle \\
 &\leq \sum_{\alpha\beta} s_\alpha(t)s_\beta(t)b_\alpha(t)b_\beta(t)\|B_\alpha\|\|B_\beta\| \\
 &\leq \left[ \sum_{\alpha} \sum_{g=1}^G \vartheta^{(m)}(t)s_\alpha^{(m)}b_\alpha^{(m)}\|B_\alpha\| \right]^2
 \end{aligned} \tag{A.22}$$

where  $b_\alpha^{(m)}$  is the maximum value that the noise assumes during the pulse,  $\vartheta^{(g)}(t) = \theta(t - t_{g-1}) - \theta(t - t_g)$  is one during the  $g$ th time interval and zero else, and where we approximated the time evolution as piecewise constant. Then, in order to guarantee convergence of the ME,

$$\begin{aligned}
 \int_0^\tau dt \|\tilde{H}_n(t)\| &\leq \int_0^\tau dt \left| \sum_{\alpha} \sum_{g=1}^G \vartheta^{(m)}(t)s_\alpha^{(m)}b_\alpha^{(m)}\|B_\alpha\| \right| \\
 &= \sum_{\alpha} b_\alpha^{(m)}\|B_\alpha\| \sum_{g=1}^G s_\alpha^{(m)} \int_{t_{g-1}}^{t_g} dt \\
 &= \sum_{\alpha} C_m \delta b_\alpha \|B_\alpha\| \sum_{g=1}^G s_\alpha^{(m)} \Delta t_g \\
 &=: N
 \end{aligned} \tag{A.23}$$

where we have expressed the in principle unknown maximum noise amplitude  $b_\alpha^{(m)}$  in terms of the root mean square value  $\delta b_\alpha$ . That is,  $b_\alpha^{(m)} = C_m \langle b_\alpha(0)^2 \rangle^{1/2} = C_m \delta b_\alpha$  for a sufficiently large value  $C_m$ . Finally, realizing that  $\delta b_\alpha^2 = \int \frac{d\omega}{2\pi} S_\alpha(\omega)$  and by the triangle inequality,

$$\begin{aligned}
 N &= C_m \sum_{\alpha} \|B_\alpha\| \left[ \int_{-\infty}^{\infty} \frac{d\omega}{2\pi} S_\alpha(\omega) \right]^{1/2} \sum_{g=1}^G s_\alpha^{(m)} \Delta t_g \\
 &\leq C_m \left[ \sum_{\alpha} \|B_\alpha\|^2 \int_{-\infty}^{\infty} \frac{d\omega}{2\pi} S_\alpha(\omega) \left( \sum_{g=1}^G s_\alpha^{(m)} \Delta t_g \right)^2 \right]^{1/2} \\
 &=: C_m \xi \\
 &\stackrel{!}{<} \pi
 \end{aligned} \tag{A.24}$$

where we have introduced the parameter  $\xi$ . Thus, the expansion converges if  $\xi < \pi/C_m$ . However, we note that in practice the rms noise amplitude  $\delta b_\alpha$  will often be infinite, limiting the usefulness of this bound for certain noise spectra.

### A.2.2 Infidelity

Again assuming a time dependence  $B_\alpha(t) = s_\alpha(t)B_\alpha$  as well as piecewise-constant control, we note that for the infidelity we have (cf. Equation 6.46)

$$\begin{aligned}
|\text{tr}(\Gamma)| &= \left| \sum_\alpha \int_0^\tau dt_2 \int_0^\tau dt_1 \langle b_\alpha(t_1) b_\alpha(t_2) \rangle \sum_k \tilde{\mathcal{B}}_{\alpha k}(t_1) \tilde{\mathcal{B}}_{\alpha k}(t_2) \right| \\
&\leq \left| \sum_\alpha \int_0^\tau dt_2 \int_0^\tau dt_1 \langle b_\alpha(t_1) b_\alpha(t_2) \rangle \sum_{g,g'=1}^G \mathfrak{g}^{(m)}(t_1) \mathfrak{g}^{(g')}(t_2) s_\alpha^{(m)} s_\alpha^{(g')} \|B_\alpha\|^2 \right| \\
&\leq \sum_\alpha \|B_\alpha\|^2 \underbrace{\langle b_\alpha^2(0) \rangle}_{\int \frac{d\omega}{2\pi} S_\alpha(\omega)} \sum_{g,g'=1}^G s_\alpha^{(m)} s_\alpha^{(g')} \left| \int_{t_{g'-1}}^{t_g} dt_2 \int_{t_{g-1}}^{t_g} dt_1 \frac{\langle b_\alpha(t_1) b_\alpha(t_2) \rangle}{|\bullet| \leq 1} \right| \\
&\leq \sum_\alpha \left[ \|B_\alpha\|^2 \int_{-\infty}^{\infty} \frac{d\omega}{2\pi} S_\alpha(\omega) \left( \sum_{g=1}^G s_\alpha^{(m)} \Delta t_g \right)^2 \right] \\
&= \xi^2,
\end{aligned} \tag{A.25}$$

where, going from the second to the third line, we have factored out the total power of noise source  $\alpha$  from the cross-correlation function,  $\langle b_\alpha(t_1) b_\alpha(t_2) \rangle = \langle b_\alpha^2(0) \rangle \frac{\langle b_\alpha(t_1) b_\alpha(t_2) \rangle}{\langle b_\alpha^2(0) \rangle}$ . Thus, the first order infidelity Equation 6.46 is upper-bounded by  $d^{-1}\xi^2$ , the same parameter also bounding the convergence of the ME, and higher orders can be neglected if  $\xi^2 \ll 1$ .

Note that similar arguments can be made for the higher orders of the ME [47]. In particular, the  $n$ th order ME term containing  $n$ -point correlation functions of the noise is of order  $\mathcal{O}(\xi^n)$  as stated in the main text.

### A.3 Concatenation of second-order filter functions

In this section, we lay out how the second-order filter functions of atomic pulse segments can be reused to compute the filter function of the concatenated sequence. While it is not possible to perform the calculation entirely without concern for the internal structure of the individual segments due to the nested time integral (cf. Equation 6.40), it is also not necessary to compute everything from scratch as we show below.

We begin by setting some notation. Wherever possible, we omit indices and thus imply matrix multiplication between objects. We assume a single noise operator and drop the corresponding index; we can easily add them again later since none of the manipulations involve the noise indices. We fully adopt the picture that control matrices can be concatenated by summing over individual time steps, which may either be single piecewise-constant segments or entire sequences, corresponding to Equation 6.36 or Equation 6.29, respectively. To make clear that the control “matrices” are in fact vectors in Liouville space, we write them as bras wherever advantageous,<sup>1</sup>

$$\tilde{\mathcal{B}}(\omega) \doteq \langle \tilde{B}(\omega) |. \tag{A.26}$$

In the following, we will consider a sequence of piecewise-constant time steps split up into subsequences (“gates”) and will deal on the one hand with quantities that depend exclusively on the internal structure of a subsequence and those that do not on the other. For the former, we will

1: Recall our convention of using Roman font for Hilbert-space operators and calligraphic font for their Liouville-space duals.

denote their internal time step by a parenthesised superscript, *e.g.*  $A^{(i)}$ , which means the  $i$ th time step of  $A$ . The latter will have no superscript as they do not depend on the internal structure. We will furthermore distinguish between *local* quantities, which do not depend on the preceding dynamics (that is, are functions of the subsequence alone), and denote the subsequence index they belong to by a parenthesised subscript, *e.g.*  $A_{(i)}$  for some quantity  $A$  of sequence  $i$ . Quantities which are *non-local* and thus depend on the preceding dynamics, but only on local quantities thereof, will have parenthesised subscripts with arrows indicating the range of the sequence, *e.g.*  $A_{(i \rightarrow 1)}$  with  $A_{(1 \rightarrow 1)} \equiv A_{(1)}$ . By contrast, non-local quantities that depend on other non-local quantities will then be denoted in a “posterior” fashion, *e.g.*,  $A_{(i|1 \rightarrow 1)}$  if  $A$  is a function of subsequence  $i$  and depends on all previous subsequences  $i - 1, \dots, 1$ . As an illustrating example, consider the first-order concatenation rule for control matrices, Equation 6.29. With this notation, we can write it as<sup>2</sup>

$$\begin{aligned} \langle\langle \tilde{B}_{(g \rightarrow 1)}(\omega) \rangle\rangle &= \sum_{g'=1}^g \langle\langle \tilde{B}_{(g'|g'-1 \rightarrow 1)}(\omega) \rangle\rangle \\ &= \langle\langle \tilde{B}_{(1)}(\omega) \rangle\rangle + \langle\langle \tilde{B}_{(2|1)}(\omega) \rangle\rangle + \langle\langle \tilde{B}_{(3|2 \rightarrow 1)}(\omega) \rangle\rangle + \dots \end{aligned} \quad (\text{A.27})$$

with

$$\langle\langle \tilde{B}_{(g|g-1 \rightarrow 1)}(\omega) \rangle\rangle := e^{i\omega t_{g-1}} \langle\langle \tilde{B}_{(g)}(\omega) \rangle\rangle Q_{(g-1 \rightarrow 1)}, \quad (\text{A.28})$$

$$Q_{(g-1 \rightarrow 1)} := \prod_{g'=g-1}^1 Q_{(g')}, \quad (\text{A.29})$$

where  $\langle\langle \tilde{B}_{(g)}(\omega) \rangle\rangle$  is the control matrix of the  $g$ th gate and  $Q_{(g)}$  the corresponding control superpropagator. For complete sequences, typically denoted by  $g = G$ , we drop the subscript,  $\langle\langle \tilde{B}_{(G \rightarrow 1)}(\omega) \rangle\rangle \equiv \langle\langle \tilde{B}(\omega) \rangle\rangle$ . Finally, we drop the specifier  $\mathcal{F}^{(2)}$  distinguishing the second- from the first-order filter function for brevity; in this section, we always mean the former.

We start from Equation 6.40, from which for reasons that will become clear shortly we define the second-order filter function by

$$\mathcal{F}_{\alpha\beta,kl}(\omega) := \mathcal{N}_{\alpha\beta,kl}(\omega) + \sum_{g=1}^G \mathcal{J}_{\alpha\beta,kl}^{(g|g-1 \rightarrow 1)}(\omega) \quad (\text{A.30})$$

with

$$\mathcal{N}_{\alpha\beta,kl}(\omega) := \sum_{g=1}^G \tilde{\mathcal{B}}_{\alpha k}^{(g|g-1 \rightarrow 1)*}(\omega) \tilde{\mathcal{B}}_{\beta l}^{(g-1 \rightarrow 1)}(\omega), \quad (\text{A.30a})$$

$$\mathcal{J}_{\alpha\beta,kl}^{(g|g-1 \rightarrow 1)}(\omega) := s_{\alpha}^{(g)} \bar{B}_{\alpha,ij}^{(g)} \bar{C}_{k,ji}^{(g \rightarrow 1)} I_{ijmn}^{(g)}(\omega) \bar{C}_{l,nm}^{(g \rightarrow 1)} \bar{B}_{\beta,mn}^{(g)} s_{\beta}^{(g)}, \quad (\text{A.30b})$$

$\bar{B}$  and  $\bar{C}$  defined in Subsection 6.2.2, and where repeated indices are contracted. Comparing to the nested time integral, the first summand in the brackets contains all contributions from complete time segments up to the one containing the inner integration variable  $t$ , whereas the second captures the final, incomplete segment with  $t_{g-1} < t \leq t_g$ . Now imagine the sequence of piecewise-constant time steps,  $g \in \{1, \dots, G\}$ , being split apart at some index  $1 < \gamma < G$  and thereby being divided into two subsequences  $g \in \{1, \dots, \gamma\}$  and  $h \in \{1, \dots, \eta\} \equiv g \in \{\gamma + 1, \dots, G\}$  with  $G = \gamma + \eta$ . Our goal is to obtain an expression for the second-order filter function  $\mathcal{F}(\omega)$  that is – as much as possible – a sum of local terms of these subsequences  $g$  and  $h$ .

2: The same definition holds for control matrices computed from Equation 6.36, in which case the subscripts would become superscripts. Similarly, sub- and superscripts can be combined.

Up to  $\gamma$ , the filter function  $\mathcal{F}_{(2 \rightarrow 1)}(\omega) \equiv \mathcal{F}(\omega)$  is simply that of the first sequence,  $\mathcal{F}_{(1)}(\omega)$ , and we thus have for  $g > \gamma^3$

$$\begin{aligned} \mathcal{F}_{(2|1)}(\omega) &= \mathcal{F}(\omega) - \mathcal{F}_{(1)}(\omega) \\ &= \sum_{g=\gamma+1}^G \left[ |\tilde{B}^{(g|g-1 \rightarrow 1)}(\omega)\rangle\langle\tilde{B}^{(g-1 \rightarrow 1)}(\omega)| + \mathcal{J}^{(g|g-1 \rightarrow 1)}(\omega) \right], \end{aligned} \quad (\text{A.31})$$

where we already plugged in Equation A.30a. We must now express the quantities  $\tilde{B}^{(g|g-1 \rightarrow 1)}(\omega)$ ,  $\tilde{B}^{(g-1 \rightarrow 1)}(\omega)$ , and  $\mathcal{J}^{(g|g-1 \rightarrow 1)}(\omega)$  locally in terms of the index  $h$ . To this end, we first write down the step-wise control matrix  $\tilde{B}^{(g|g-1 \rightarrow 1)}(\omega)$  in the second sequence and split off phases and propagators from the first sequence,

$$\begin{aligned} \langle\tilde{B}^{(g|g-1 \rightarrow 1)}(\omega)| &= e^{i\omega t_g} \langle\tilde{B}^{(g)}(\omega)| \mathcal{Q}^{(g-1 \rightarrow 1)} \\ &= e^{i\omega(t_\gamma + t_h)} \langle\tilde{B}_{(2)}^{(h)}(\omega)| \mathcal{Q}_{(2)}^{(h-1)} \mathcal{Q}_{(1)} \\ &= e^{i\omega\tau_{(1)}} \langle\tilde{B}_{(2)}^{(h|h-1 \rightarrow 1)}(\omega)| \mathcal{Q}_{(1)} \\ &= \langle\tilde{B}_{(2|1)}^{(h|h-1 \rightarrow 1)}(\omega)|, \end{aligned} \quad (\text{A.32})$$

where  $\tau_{(1)} = t_\gamma$  is the duration of the first sequence and  $h = g - \gamma$ . Next, we consider the cumulative control matrix  $\tilde{B}^{(g-1 \rightarrow 1)}(\omega)$ . Because in the total sequence it is given by the sum over all  $\tilde{B}^{(g'|g' \rightarrow 1)}(\omega)$  up to  $g-1$ , we can split off the complete control matrix of the first sequence and express the remainder by summing over  $\tilde{B}_{(2|1)}^{(h)}(\omega)$  from Equation A.32:

$$\begin{aligned} \langle\tilde{B}^{(g-1 \rightarrow 1)}(\omega)| &= \langle\tilde{B}_{(1)}(\omega)| + e^{i\omega\tau_{(1)}} \sum_{h'=1}^{g-1-\gamma} \langle\tilde{B}_{(2)}^{(h'|h' \rightarrow 1)}(\omega)| \mathcal{Q}_{(1)} \\ &= \langle\tilde{B}_{(1)}(\omega)| + e^{i\omega\tau_{(1)}} \langle\tilde{B}_{(2)}^{(h-1 \rightarrow 1)}(\omega)| \mathcal{Q}_{(1)} \\ &= \langle\tilde{B}_{(2 \rightarrow 1)}^{(h-1 \rightarrow 1)}(\omega)| \end{aligned} \quad (\text{A.33})$$

Finally, we need to unravel  $\mathcal{J}^{(g|g-1 \rightarrow 1)}(\omega)$ . We start from Equation 6.36, consider a time step  $g \geq \gamma$  in the second sequence with  $h = g - \gamma$ , and rewrite

$$\begin{aligned} \mathcal{J}_{kl}^{(g|g-1 \rightarrow 1)}(\omega) &= s^{(g)} \tilde{B}_{ij}^{(g)} \tilde{C}_{kji}^{(g \rightarrow 1)} I_{ijmn}^{(g)}(\omega) \tilde{C}_{lmn}^{(g \rightarrow 1)} \tilde{B}_{mn}^{(g)} s^{(g)} \\ &= s_{(2)}^{(h)} \tilde{B}_{(2),ij}^{(h)} \tilde{C}_{(2 \rightarrow 1),kji}^{(h \rightarrow 1)} I_{(2),ijmn}^{(h)}(\omega) \tilde{C}_{(2 \rightarrow 1),lmn}^{(h \rightarrow 1)} \tilde{B}_{(2),mn}^{(h)} s_{(2)}^{(h)} \\ &= \mathcal{J}_{(2|1),kl}^{(h|h-1 \rightarrow 1)}(\omega) \end{aligned} \quad (\text{A.34})$$

because all quantities except for  $\tilde{C}_{(2|1)}^{(g)}$  depend on their timestep  $g$  alone, and where  $i, j, m, n$  index the Hilbert space dimensions of the operators, while  $k, l$  are the usual indices for the basis elements and therefore Liouville space dimensions. On that term, we can factor out the propagators of the first complete sequence,<sup>4</sup>

$$\tilde{C}_{(2 \rightarrow 1),kij}^{(h \rightarrow 1)} = \left[ V_{(2)}^{(h)\dagger} \mathcal{Q}_{(2)}^{(h-1 \rightarrow 1)} \mathcal{Q}_{(1)} C_k \mathcal{Q}_{(1)}^\dagger \mathcal{Q}_{(2)}^{(h-1 \rightarrow 1)\dagger} V_{(2)}^{(h)} \right]_{ij}. \quad (\text{A.35})$$

We can now finally put all pieces together and, starting from Equation A.31, plug in Equations A.32 to A.34, so that we obtain<sup>5</sup>

3: We drop indices for legibility as stated above;  $\mathcal{J}^{(g|g-1 \rightarrow 1)}(\omega)$  is a matrix on Liouville space, whereas  $\tilde{B}^{(g|g-1 \rightarrow 1)}(\omega)$  and  $\tilde{B}^{(g-1 \rightarrow 1)}(\omega)$  are Liouville-space row vectors and their product here is an outer product,  $|\tilde{B}^{(g|g-1 \rightarrow 1)}(\omega)\rangle\langle\tilde{B}^{(g-1 \rightarrow 1)}(\omega)|$ , resulting in a matrix on Liouville space.

4: Note that the  $\mathcal{Q}_{(i)}$  here are Hilbert space propagators, not their Liouville space counter parts  $\mathcal{Q}_{(i)}$ , and that  $\mathcal{Q}_{(2)}^{(h-1 \rightarrow 1)} \equiv \mathcal{Q}_{h-1}$  in the notation of Subsection 6.2.1.

5: Recall that  $\mathcal{Q}$  is the Liouville representation of the unitary operator  $Q$  and as such – and because our chosen basis  $C$  is Hermitian – is an orthogonal matrix for which  $\mathcal{Q}^\top \mathcal{Q} = \mathbb{1}$ .

$$\begin{aligned}
 \mathcal{F}_{(2|1)}(\omega) &= \sum_{h=1}^{\eta} \left[ |\tilde{B}_{(2|1)}^{(h|h-1 \rightarrow 1)}(\omega)\rangle\langle\tilde{B}_{(2 \rightarrow 1)}^{(h-1 \rightarrow 1)}(\omega)| + \mathcal{J}_{(2|1)}^{(h|h-1 \rightarrow 1)}(\omega) \right] \\
 &= \sum_{h=1}^{\eta} \left\{ e^{-i\omega\tau_{(1)}} \mathcal{Q}_{(1)}^{\top} |\tilde{B}_{(2)}^{(h|h-1 \rightarrow 1)}(\omega)\rangle \right. \\
 &\quad \times \left[ \langle\tilde{B}_{(1)}(\omega)| + e^{i\omega\tau_{(1)}} \langle\tilde{B}_{(2)}^{(h-1 \rightarrow 1)}(\omega)| \mathcal{Q}_{(1)} \right] + \mathcal{J}_{(2|1)}^{(h|h-1 \rightarrow 1)}(\omega) \left. \right\}. \tag{A.36}
 \end{aligned}$$

To simplify the unwieldy first summand in the curly braces further, we expand the product,

$$\begin{aligned}
 &e^{-i\omega\tau_{(1)}} \mathcal{Q}_{(1)}^{\top} |\tilde{B}_{(2)}^{(h|h-1 \rightarrow 1)}(\omega)\rangle \left[ \langle\tilde{B}_{(1)}(\omega)| + e^{i\omega\tau_{(1)}} \langle\tilde{B}_{(2)}^{(h-1 \rightarrow 1)}(\omega)| \mathcal{Q}_{(1)} \right] \\
 &= e^{-i\omega\tau_{(1)}} \mathcal{Q}_{(1)}^{\top} |\tilde{B}_{(2)}^{(h|h-1 \rightarrow 1)}(\omega)\rangle\langle\tilde{B}_{(1)}(\omega)| \\
 &\quad + \mathcal{Q}_{(1)}^{\top} |\tilde{B}_{(2)}^{(h|h-1 \rightarrow 1)}(\omega)\rangle\langle\tilde{B}_{(2)}^{(h-1 \rightarrow 1)}(\omega)| \mathcal{Q}_{(1)}. \tag{A.37}
 \end{aligned}$$

If we now pull in the sum over the time steps  $h$ , we can identify in the first term the control matrix and Equation A.27, and in the second the contribution from complete segments to the second-order filter function, Equation A.30a).<sup>6</sup>

6: We write explicitly  $\langle\tilde{B}_{(1 \rightarrow 1)}(\omega)|$  to emphasize that this is the *cumulative* control matrix.

$$\begin{aligned}
 &\sum_{h=1}^{\eta} (\text{r.h.s Equation A.37}) \\
 &= e^{-i\omega\tau_{(1)}} \mathcal{Q}_{(1)}^{\top} |\tilde{B}_{(2)}(\omega)\rangle\langle\tilde{B}_{(1 \rightarrow 1)}(\omega)| + \mathcal{Q}_{(1)}^{\top} \mathcal{N}_{(2)}(\omega) \mathcal{Q}_{(1)}. \tag{A.38}
 \end{aligned}$$

As a last step, we recognize that the bra in the first term is nothing else but Equation A.28 so that we can write the filter function succinctly as

$$\begin{aligned}
 \mathcal{F}_{(2|1)}(\omega) &= |\tilde{B}_{(2|1)}(\omega)\rangle\langle\tilde{B}_{(1 \rightarrow 1)}(\omega)| + \mathcal{Q}_{(1)}^{\top} \mathcal{N}_{(2)}(\omega) \mathcal{Q}_{(1)} + \sum_{h=1}^{\eta} \mathcal{J}_{(2|1)}^{(h|h-1 \rightarrow 1)}(\omega) \\
 &= \mathcal{N}_{(2|1)}(\omega) + \sum_{h=1}^{\eta} \mathcal{J}_{(2|1)}^{(h|h-1 \rightarrow 1)}(\omega). \tag{A.39}
 \end{aligned}$$

In Equation A.39, all terms except the last are known ahead of time if the first- and second-order filter functions of the subsequences as well as the control matrix of the concatenated sequence have been computed. We can extend this result to sequences consisting of an arbitrary number of  $G$  subsequences with lengths  $\{\eta_g\}_{g=1}^G$  by recursively shifting indices in Equation A.39 up by one and subsequently adding  $\mathcal{F}_{(2|1)}(\omega)$ , allowing us to write the concatenation rule for second-order filter functions as

$$\mathcal{F}(\omega) = \sum_{g=1}^G \mathcal{F}_{(g|g-1 \rightarrow 1)}(\omega) \tag{A.40}$$

$$= \sum_{g=1}^G \left[ \mathcal{N}_{(g|g-1 \rightarrow 1)}(\omega) + \sum_{h_g=1}^{\eta_g} \mathcal{J}_{(g|g-1 \rightarrow 1)}^{(h_g|h_g-1 \rightarrow 1)}(\omega) \right] \tag{A.40a}$$

with

$$\begin{aligned}
 &\mathcal{N}_{(g|g-1 \rightarrow 1)}(\omega) \\
 &= |\tilde{B}_{(g|g-1 \rightarrow 1)}(\omega)\rangle\langle\tilde{B}_{(g-1 \rightarrow 1)}(\omega)| + \mathcal{Q}_{(g-1 \rightarrow 1)}^{\top} \mathcal{N}_{(g)}(\omega) \mathcal{Q}_{(g-1 \rightarrow 1)} \tag{A.40b}
 \end{aligned}$$

and

$$\begin{aligned} \mathcal{J}_{(g|g-1 \rightarrow 1),kl}^{(h|h-1 \rightarrow 1)}(\omega) \\ = s_{(g)}^{(h)} \bar{B}_{(g),ij}^{(h)} \bar{C}_{(g \rightarrow 1),kji}^{(h \rightarrow 1)} I_{(g),ijmn}^{(h)}(\omega) \bar{C}_{(g \rightarrow 1),lmn}^{(h \rightarrow 1)} \bar{B}_{(g),mn}^{(h)} s_{(g)}^{(h)}. \end{aligned} \quad (\text{A.40c})$$

Equation A.40 is our final result. Before we analyze it in more detail, let us first briefly discuss the special case where  $G = 1$ . Then,  $\mathcal{Q}_{(0)} = \mathbb{1}$ ,  $\langle \tilde{B}_{(0)} | = 0$ , and hence  $|\tilde{B}_{(1)}(\omega)\rangle \langle \tilde{B}_{(0)}(\omega)| = 0$  so that Equation A.40 reduces to Equation A.30 as it should.

To compute the second-order filter function of a sequence of quantum gates most efficiently, Equation A.40 suggests the following procedure:

1. Compute the control matrix for all gates individually. This requires the quantities  $V_{(g)}^{(h)}$ ,  $\bar{B}_{(g)}^{(h)}$ , and  $Q_{(g)}^{(h)}$  to be computed, allowing them to be reused in Equation A.35.
2. Compute the second-order filter function for all gates individually. This requires the quantities  $I_{(g)}^{(h)}(\omega)$  (Equation 6.41) and  $\mathcal{N}_{(g)}(\omega)$  to be computed, allowing them to be reused in Equations A.40b and A.40c, respectively.
3. Compute the control matrix of the entire sequence. This requires the quantities  $\bar{B}_{(g|g-1 \rightarrow 1)}(\omega)$  and  $\bar{B}_{(g \rightarrow 1)}(\omega)$  to be computed, allowing them to be reused in Equation A.40b.

In this way, the only computations that need to be performed once for each gate  $g$  to evaluate Equation A.40 are the outer product and matrix multiplications in Equation A.40b. Additionally, for every time step of the entire sequence, the quantity  $\bar{C}_{(g \rightarrow 1)}^{(h \rightarrow 1)}$  needs to be computed following Equation A.35, the contraction in Equation A.40c performed, and finally  $\mathcal{J}_{(g|g-1 \rightarrow 1)}^{(h|h-1 \rightarrow 1)}(\omega)$  added to the result. In total, this requires  $\mathcal{O}(G + H)$  computations, where  $H = \sum_{g=1}^G n_g$  is the total number of time steps, yielding a favorable linear scaling in  $H$  compared to a naive approach that is  $\mathcal{O}(H^2)$  due to the nested time integral.

## A.4 Monte Carlo and GKSL master equation simulations

In this section, we lay out two common time-domain simulation methods of noisy quantum dynamics for completeness; direct simulation of the Gorini-Kossakowski-Sudarshan-Lindblad (GKSL) master equation and stochastic Monte Carlo (MC) simulation of the Schrödinger equation. These can serve as alternative and complementary approaches to the filter-function formalism presented in Part IV. All simulations were performed using the `lindblad_mc_tools` software package written during the course of the present thesis [49].

### A.4.1 Simulation methods

To simulate a quantum system under the influence of Markovian (white) noise, a common approach is the GKSL master equation [50, 51]. Here, we give it in superoperator form. We represent linear maps  $\mathcal{A} : \rho \rightarrow$



$\mathcal{A}(\rho)$  by matrices in the Liouville representation following Equation 6.1 and operators as column vectors (*i.e.*, generalized Bloch vectors) as

$$\rho_i := \text{tr}(\sigma_i \rho), \quad (\text{A.41})$$

allowing us to write the Lindblad equation

$$\frac{d}{dt}\rho(t) = -i[H(t), \rho(t)] + \sum_{\alpha} \gamma_{\alpha} \left( L_{\alpha} \rho(t) L_{\alpha}^{\dagger} - \frac{1}{2} \{ L_{\alpha}^{\dagger} L_{\alpha}, \rho(t) \} \right) \quad (\text{A.42})$$

as a linear differential equation in matrix form,

$$\frac{d}{dt}\rho_i(t) = \sum_j \left( -i\mathcal{H}_{ij}(t) + \sum_{\alpha} \gamma_{\alpha} \mathcal{D}_{\alpha,ij} \right) \rho_j(t). \quad (\text{A.43})$$

Here,  $\mathcal{H}_{ij}(t) = \text{tr}(\sigma_i [H(t), \sigma_j])$  and  $\mathcal{D}_{\alpha,ij} = \text{tr}(\sigma_i L_{\alpha} \sigma_j L_{\alpha}^{\dagger} - \frac{1}{2} \sigma_i \{ L_{\alpha}^{\dagger} L_{\alpha}, \sigma_j \})$ . The  $\gamma_{\alpha}$  are coupling constants to the noise bath and can be related to the amplitude of the power spectral density (PSD). For Hermitian  $L_{\alpha}$ , the solution to Equation A.42 is a completely-positive trace preserving (CPTP) as well as unital map. Equation A.43 is readily solved under the approximation of piecewise constant timesteps  $\Delta t_g = t_g - t_{g-1}$  and one obtains for the complete superpropagator

$$\mathcal{U}(t_g, t_{g-1}) = \exp \left\{ \left( -i\mathcal{H}(t_g) + \sum_{\alpha} \gamma_{\alpha} \mathcal{D}_{\alpha} \right) \Delta t_g \right\} \quad (\text{A.44})$$

with

$$\mathcal{U}(\tau) = \prod_{g=G}^1 \mathcal{U}(t_g, t_{g-1}). \quad (\text{A.45})$$

The entanglement fidelity can then be computed as  $F_{\text{ent}} = d^{-2} \text{tr}(Q^{\dagger} \mathcal{U})$ , where  $Q$  is the superpropagator due to the Hamiltonian evolution alone (*i.e.*, the ideal evolution without noise), and  $F_{\text{avg}}$  obtained using Equation 6.45.

In a MC simulation, we work with single realizations of the noise Hamiltonian in Equation 6.3 and solve the Schrödinger equation governed by it. This results in unitary dynamics. The ensemble-averaged dynamics are then obtained by randomly drawing many realizations, solving the Schrödinger equation and computing the desired quantities for each, before finally averaging over all realizations. To sample the PSD faithfully, the piecewise constant time step needs to be significantly smaller than in a noise-free simulation in order to resolve high frequencies of the noise (*cf.* Chapter 2). In practice, we generate time traces of the noise fields by drawing pseudo-random numbers from a distribution whose PSD is  $S(f)$ . To do this, we draw complex, normally distributed samples in frequency space (*i.e.* white noise), scale it with the amplitude spectral density (ASD), and finally perform the inverse Fourier transform. We then solve the Schrödinger equation by diagonalizing the full Hamiltonian  $H(t) = H_c(t) + H_n(t)$  and computing the propagator for one noise realization as

$$U(t) = \prod_g V^{(g)} \exp(-i\Omega^{(g)} \Delta t_{\text{MC}}) V^{(g)\dagger}, \quad (\text{A.46})$$

where  $V^{(g)}$  is the unitary matrix of eigenvectors of  $H(t)$  during time segment  $g$  and  $\Omega^{(g)}$  the diagonal matrix of eigenvalues. We can then obtain an estimate for the entanglement fidelity  $F_{\text{ent}}$  as

$$\langle F_{\text{ent}} \rangle = \left\langle \left| \text{tr}(Q^{\dagger} U(\tau)) \right|^2 \right\rangle, \quad (\text{A.47})$$

and  $F_{\text{avg}}$  again from Equation 6.45. Here,  $Q \equiv U_c(t = \tau)$  is the noise-free propagator at time  $\tau$  of completion of the circuit and  $\langle \cdot \rangle$  denotes the ensemble average over  $N$  Monte Carlo realizations of Equation A.46, *i.e.*,  $\langle A \rangle = N^{-1} \sum_{i=1}^N A_i$ . The standard error of the mean can be obtained as  $\sigma_{\langle F_{\text{avg}} \rangle} = \sigma_{F_{\text{avg}}} / \sqrt{N}$  with  $\sigma_{F_{\text{avg}}}$  the standard deviation over the Monte Carlo traces.

## A.5 Fidelity validation

In this section, we lay out in more detail how the fidelity of the optimized S- $T_0$  qubit gates from Reference 45 was calculated using filter functions, as well as validate the fidelities computed for the QFT algorithm in Section 9.4 using the methods presented in Section A.4.

### A.5.1 Singlet-Triplet Gate Fidelity

In two singlet-triplet qubits, angular momentum conservation suppresses occupancy of states with non-vanishing magnetic spin quantum number  $m_s$  so that the total accessible state space of dimension  $d = 6$  is spanned by  $\{|\uparrow\downarrow\uparrow\downarrow\rangle, |\uparrow\downarrow\downarrow\uparrow\rangle, |\downarrow\uparrow\uparrow\downarrow\rangle, |\downarrow\uparrow\downarrow\uparrow\rangle, |\uparrow\uparrow\downarrow\downarrow\rangle, |\downarrow\downarrow\uparrow\uparrow\rangle\}$ . A straightforward method to single out the computational subspace (CS) dynamics from those on the whole space would be to simply project the error transfer matrix  $\tilde{\mathcal{U}} \approx \mathbb{1} + \mathcal{K}$  with  $\mathcal{K}$  the cumulant function onto the CS as proposed by Wood and Gambetta [52], that is calculate the fidelity as  $F_{\text{ent}} = d_c^{-2} \text{tr}(\Pi_c \tilde{\mathcal{U}})$  where  $\Pi_c$  is the Liouville representation of the projector onto the CS and  $d_c = 4$  the dimension of the CS. However, here we use a more involved procedure in order to gain more insight from the error transfer matrix as well as to obtain a better comparison to the fidelities computed by Cerfontaine et al. [45], who map the final  $6 \times 6$  propagator to the closest unitary on the  $4 \times 4$  CS during their Monte Carlo simulation.

To calculate the fidelity of the target unitary on the  $4 \times 4$  CS, we thus construct an orthonormal operator basis  $\mathbf{C}$  of the full  $6 \times 6$  space that is partitioned into elements which are nontrivial only on the CS on the one hand and elements which are nontrivial only on the remaining space on the other such that  $\mathbf{C} = \mathbf{C}^c \cup \mathbf{C}^\ell$ . Using such a basis, we can then trace only over CS elements of the error transfer matrix  $\tilde{\mathcal{U}}$  in Equation 6.46 to obtain the fidelity of the gate on the CS. Moreover, we retain the opportunity to characterize the gates on the basis of the Pauli matrices.

Since there is no obvious way to extend the Pauli basis for two qubits to the complete space we proceed as follows: For the CS, we pad the two-qubit Pauli basis with zeros on the leakage levels, *i.e.*,

$$C_i^c \doteq \begin{matrix} & |\uparrow\downarrow\uparrow\downarrow\rangle & |\downarrow\downarrow\uparrow\uparrow\rangle \\ \begin{matrix} |\uparrow\downarrow\uparrow\downarrow\rangle \\ |\downarrow\downarrow\uparrow\uparrow\rangle \end{matrix} & \begin{pmatrix} P_i & 0 & 0 \\ 0 & 0 & 0 \\ 0 & 0 & 0 \end{pmatrix} \end{matrix}, \quad i \in \{0, \dots, 15\}, \quad (\text{A.48})$$

where the  $P_i$  are normalized two-qubit Pauli matrices (*cf.* Equation 6.54) in the basis  $\{|\uparrow\downarrow\uparrow\downarrow\rangle, |\uparrow\downarrow\downarrow\uparrow\rangle, |\downarrow\uparrow\uparrow\downarrow\rangle, |\downarrow\uparrow\downarrow\uparrow\rangle\}$ . To complete the basis we require an additional 20 elements orthogonal to the 16 padded Pauli matrices. We obtain the remaining elements by first expanding the  $C_i^c$  in an arbitrary basis  $\{\Lambda_i\}_{i=0}^{35}$  of the complete space (we choose a generalized

Gell-Mann (GGM) basis, Equation 6.55, for simplicity), yielding a  $16 \times 36$  matrix of expansion coefficients:

$$M_{ij} = \text{tr}(C_i^c \Lambda_j). \quad (\text{A.49})$$

We then compute an orthonormal vector basis  $V$  (a matrix of size  $36 \times 20$ ) for the null space of  $M$  using singular value decomposition  $M = U\Sigma V^\dagger$  and acquire the corresponding basis matrices as

$$C_i^\ell = \sum_j \Lambda_j V_{ji}, \quad i \in \{0, \dots, 19\}. \quad (\text{A.50})$$

Finally, to account for the fact that Cerfontaine et al. [45] map the total propagator to the closest unitary on the CS, we exclude the identity Pauli element  $C_0^c \propto \text{diag}(1, 1, 1, 1, 0, 0)$  from the trace over the computational subspace part of  $\tilde{U}$  represented in the basis  $C = C^c \cup C^\ell$  when calculating the fidelity,

$$F_{\text{ent}} = \frac{1}{16} \sum_{i=1}^{15} \tilde{U}_{ii}, \quad (\text{A.51})$$

since for unitary operations on the CS we have  $\mathcal{K}_{00} \approx 1 - \tilde{U}_{00} = 1 - \text{tr}(C_0^c \tilde{U} C_0^c) = 0$ . Hence, excluding  $\tilde{U}_{00}$  from the trace corresponds to partially disregarding non-unitary components of the error channel on the computational subspace. Although not the only element that differs compared to the closest subspace unitary,  $\mathcal{K}_{00}$  contains the most obvious contribution, whereas those of other elements are more difficult to disentangle into unitary and non-unitary components.

Similar to the fidelity, we also obtain the canonical filter function shown in panel (b) of Figure 9.1 by summing only over columns one through 15 of the control matrix,  $F_{\epsilon_{ij}}(\omega) = \sum_{k=1}^{15} |\tilde{B}_{\epsilon_{ij}k}(\omega)|^2$ . In fact, including the first column, corresponding to the padded identity matrix  $C_0^c$ , in the filter function removes the DCG character of  $F_{\epsilon_{12}}(\omega)$  and  $F_{\epsilon_{34}}(\omega)$ , which instead approach a constant level of around 20 (note that the filter function is dimensionless in our units) at zero frequency. This is consistent with the fact that the gates were optimized using quasistatic and fast white noise contributions to the fidelity after mapping to the closest unitary on the computational subspace. We have performed Monte Carlo resimulations that support this reading. In Figure A.1 we show the filter functions once including and once excluding the contributions from  $C_0^c$ .

### A.5.2 GRAPE-optimized gate set and validation of QFT fidelities

In this section we give details on the GRAPE-optimized pulses for the gate set  $G = \{X_i(\pi/2), Y_i(\pi/2), \text{CR}_{ij}(\pi/2^3)\}$  used in Section 9.4 to simulate a QFT algorithm, and validate the fidelities using time-domain simulations. As mentioned in the main text, we consider a toy Rabi driving model with in-phase/quadrature (IQ) single-qubit control and exchange to mediate inter-qubit coupling. Cast in the language of quantum optimal control theory this translates to a vanishing drift (static) Hamiltonian,  $H_d = 0$ , and a control Hamiltonian in the rotating frame given by

$$H_c(t) = H_c^{(0)}(t) \otimes 1 + 1 \otimes H_c^{(1)}(t) + H_c^{(01)}(t), \quad (\text{A.52})$$

$$H_c^{(i)}(t) = I_i(t) \sigma_x^{(i)} + Q_i(t) \sigma_y^{(i)}, \quad (\text{A.53})$$

$$H_c^{(ij)}(t) = J_{ij}(t) \sigma_z^{(i)} \otimes \sigma_z^{(j)}, \quad (\text{A.54})$$

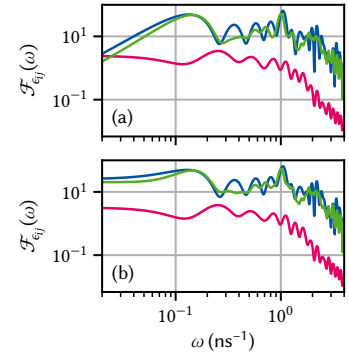


**Figure A.1:** Filter functions of the voltage detunings  $\epsilon_{ij}$  excluding (a) and including (b) the zero-padded identity matrix basis element  $C_0^c \propto \text{diag}(1, 1, 1, 1, 0, 0)$  for the computational subspace. Evidently, including  $C_0^c$  removes the dynamically corrected gate (DCG) character, namely that  $F_{\epsilon_{ij}}(\omega) \rightarrow 0$  as  $\omega \rightarrow 0$ , of the gates but has little effect on the high-frequency behavior. As the pulse optimization minimizes, among other figures of merit, the infidelity of the final propagator mapped to the closest unitary on the computational subspace due to quasistatic and fast white noise, this indicates that excluding  $C_0^c$  from the filter function corresponds to partially neglecting non-unitary components of the propagator on the computational subspace.

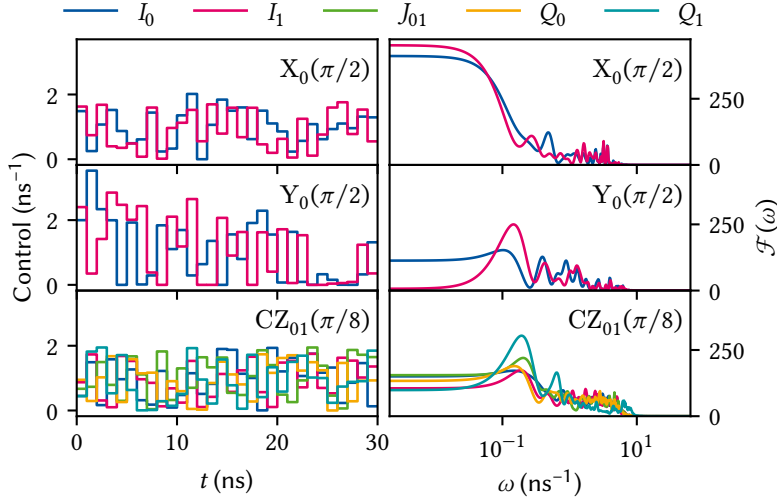


**Figure A.2:** Control fields (top row) and corresponding filter functions (bottom row) of the gradient ascent pulse engineering (GRAPE)-optimized pulses in G. (a),(b)  $X_0(\pi/2)$ ; (c),(d)  $Y_0(\pi/2)$ ; (e),(f)  $CZ_{01}(\pi/8)$ . Note that the optimization is neither very sophisticated nor realistic as the algorithm only maximizes the systematic (coherent) fidelity  $\text{tr}(UQ_{\text{targ}}^\dagger)/d$  and the randomly distributed initial control amplitudes are not subject to any constraints.

where  $I_i(t)$  and  $Q_i(t)$  are the in-phase and quadrature pulse envelopes and  $\sigma_{x,y}^{(i)}$  are the Pauli matrices acting on the  $i$ th and extended trivially to the other qubit. For simplicity, we assume periodic boundary conditions so that qubits 1 and 4 are nearest neighbors as well. As our goal is only of illustrative nature and not to provide a detailed gate optimization, we obtain the controls  $\{I_0(t), Q_0(t), I_1(t), Q_1(t), J_{12}(t)\}$  for the gate set G using the GRAPE algorithm implemented in QuTiP [53] initialized with randomly distributed amplitudes. The resulting pulses and the corresponding filter functions for the relevant noise operators are shown in Figure A.2.

We now perform GKSL master equation and MC simulations using the methods laid out in Subsection A.4.1 to verify the fidelities predicted for the QFT circuit in Section 9.4. We focus on noise exclusively on the third qubit, entering through the noise operator  $B_\alpha \equiv \sigma_y^{(3)}$ . We assemble the QFT circuit discussed in the main text from the gate set G, obtaining the control Hamiltonian

$$H_c(t) = \sum_{\langle i,j \rangle} I_i(t)\sigma_x^{(i)} + Q_i(t)\sigma_y^{(i)} + J_{ij}(t)\sigma_z^{(i)} \otimes \sigma_z^{(j)}. \quad (\text{A.55})$$

Similarly, we define the noise Hamiltonian as

$$H_n(t) = \sum_{\langle i,j \rangle} b_I(t)\sigma_x^{(i)} + b_Q(t)\sigma_y^{(i)} + b_J(t)\sigma_z^{(i)} \otimes \sigma_z^{(j)} \quad (\text{A.56})$$

with the noise fields  $b_\alpha(t)$  for  $\alpha \in \{I, Q, J\}$ . For the GKSL master equation, we set  $L_\alpha \equiv \sigma_y^{(3)}$  as well as  $\gamma_\alpha \equiv S_0/2$  with  $S_0$  the amplitude of the one-sided noise PSD so that  $S(\omega) = S_0$ . For the MC simulation, we explicitly generate time traces of  $b_Q(t)$  (cf. Equation A.56). We choose an oversampling factor of 16 so that the time discretization of the simulation is  $\Delta t_{\text{MC}} = \Delta t/16 = 62.5 \text{ ps}$  ( $\Delta t = 1 \text{ ns}$  is the time step of the pulses used in the FF simulation), leading to a highest resolvable frequency of  $f_{\text{max}} = 16 \text{ GHz}$ . Conversely, we increase the frequency resolution by sampling a time trace longer by a given factor, giving frequencies below  $f_{\text{min}}$  (16 kHz for pink, 0 Hz for white noise) weight zero, and truncating it to the number of time steps in the algorithm times the oversampling factor. This yields a time trace with frequencies  $f \in [f_{\text{min}}, f_{\text{max}}]$  and a given resolution (we choose  $\Delta f = 160 \text{ Hz}$ ). For reference, we show the fidelity filter functions for the circuit with and without echo pulses in

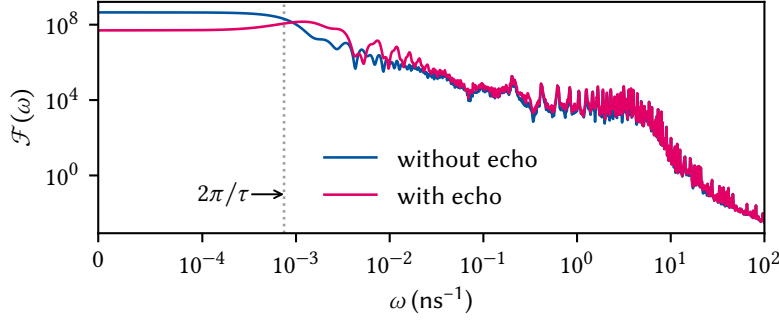


**Figure A.3:** Filter functions for noise operator  $\sigma_y^{(3)}$  for the QFT circuit without (blue) and with (magenta) additional echo pulses. Introducing the echoes shifts spectral weight towards higher frequencies, reducing the DC level of the filter function by two orders of magnitude and thus leading to an improved fidelity for  $1/f$  noise.

**Table A.1:** Infidelities  $I_{\text{avg}} = 1 - F_{\text{avg}}$  of the QFT circuit due to noise on  $\sigma_y^{(3)}$ . MC values are averages over  $N = 1000$  random traces and have a relative error of 3%. We included frequencies in the range of  $\omega \in [0, 100] \text{ ns}^{-1}$  for white noise, and  $\omega \in [100 \text{ ms}^{-1}, 100 \text{ ns}^{-1}]$  for pink noise. FF values are computed with  $n_\omega = 1000$  samples logarithmically distributed over the same interval. Prefactors in the power law  $S(\omega) = A\omega^\alpha$  are  $2 \times 10^{-6} \text{ ns}^{-1}$  and  $10^{-9} \text{ ns}^{-2}$ , respectively.

METHOD	WHITE NOISE		$1/f$ NOISE	
	WITHOUT ECHO	WITH ECHO	WITHOUT ECHO	WITH ECHO
GKSL	$8.38 \times 10^{-3}$	$8.38 \times 10^{-3}$	—	—
MC	$8.74 \times 10^{-3}$	$8.00 \times 10^{-3}$	$2.11 \times 10^{-2}$	$4.28 \times 10^{-3}$
FF	$8.38 \times 10^{-3}$	$8.40 \times 10^{-3}$	$2.12 \times 10^{-2}$	$4.46 \times 10^{-3}$

this frequency band in Figure A.3.

Table A.1 compares the infidelities  $I = 1 - F$  from GKSL and MC simulations to the filter function predictions following Equation 6.48. Note that the precise value of the filter function result depends quite sensitively on the frequency sampling due to the sharp peaks in the gigahertz range (Figure A.3). As the table shows, both the GKSL and the MC calculations agree well with the predictions made by our filter-function formalism.

# Bibliography

- [1] Jonathan P. Dowling and Gerard J. Milburn. “Quantum Technology: The Second Quantum Revolution.” In: *Philosophical Transactions of the Royal Society of London. Series A: Mathematical, Physical and Engineering Sciences* 361.1809 (Aug. 15, 2003). Ed. by A. G. J. MacFarlane, pp. 1655–1674. DOI: [10.1098/rsta.2003.1227](https://doi.org/10.1098/rsta.2003.1227) (cited on page 2).
- [2] Alain Aspect. *Einstein and the Quantum Revolutions*. Trans. by David Kaiser Translated by Teresa Laverder Fagan. The France Chicago Collection. Chicago, IL: University of Chicago Press, Oct. 2024. 112 pp. (cited on page 2).
- [3] A. A. Clerk et al. “Introduction to Quantum Noise, Measurement, and Amplification.” In: *Reviews of Modern Physics* 82.2 (Apr. 15, 2010), pp. 1155–1208. DOI: [10.1103/RevModPhys.82.1155](https://doi.org/10.1103/RevModPhys.82.1155) (cited on pages 2, 4).
- [4] Tobias Hangleiter et al., *Python-Spectrometer* version 2024.11.1, Nov. 21, 2024. Zenodo. DOI: [10.5281/ZENODO.13789861](https://doi.org/10.5281/ZENODO.13789861), (cited on pages 3, 11).
- [5] Gerardo A. Paz-Silva, Leigh M. Norris, and Lorenza Viola. “Multiqubit Spectroscopy of Gaussian Quantum Noise.” In: *Physical Review A* 95.2 (Feb. 23, 2017), p. 022121. DOI: [10.1103/PhysRevA.95.022121](https://doi.org/10.1103/PhysRevA.95.022121) (cited on page 4).
- [6] Eric W. Weisstein. *Root-Mean-Square*. URL: <https://mathworld.wolfram.com/Root-Mean-Square.html> (visited on 04/21/2025) (cited on page 4).
- [7] Gonzalo A. Álvarez and Dieter Suter. “Measuring the Spectrum of Colored Noise by Dynamical Decoupling.” In: *Physical Review Letters* 107.23 (Nov. 30, 2011), p. 230501. DOI: [10.1103/PhysRevLett.107.230501](https://doi.org/10.1103/PhysRevLett.107.230501) (cited on page 4).
- [8] P Szańkowski et al. “Environmental Noise Spectroscopy with Qubits Subjected to Dynamical Decoupling.” In: *Journal of Physics: Condensed Matter* 29.33 (Aug. 23, 2017), p. 333001. DOI: [10.1088/1361-648X/aa7648](https://doi.org/10.1088/1361-648X/aa7648) (cited on pages 4, 10).
- [9] O. E. Dial et al. “Charge Noise Spectroscopy Using Coherent Exchange Oscillations in a Singlet-Triplet Qubit.” In: *Physical Review Letters* 110.14 (Apr. 5, 2013), p. 146804. DOI: [10.1103/PhysRevLett.110.146804](https://doi.org/10.1103/PhysRevLett.110.146804) (cited on page 4).
- [10] Elliot J. Connors et al. “Charge-Noise Spectroscopy of Si/SiGe Quantum Dots via Dynamically-Decoupled Exchange Oscillations.” In: *Nature Communications* 13.1 (Dec. 2022), p. 940. DOI: [10.1038/s41467-022-28519-x](https://doi.org/10.1038/s41467-022-28519-x) (cited on page 4).
- [11] Norbert Wiener. “Generalized Harmonic Analysis.” In: *Acta Mathematica* 55 (none Jan. 1930), pp. 117–258. DOI: [10.1007/BF02546511](https://doi.org/10.1007/BF02546511) (cited on pages 4, 6).
- [12] A. Khintchine. “Korrelationstheorie der stationären stochastischen Prozesse.” In: *Mathematische Annalen* 109.1 (Dec. 1, 1934), pp. 604–615. DOI: [10.1007/BF01449156](https://doi.org/10.1007/BF01449156) (cited on pages 4, 6).
- [13] Arian Vezvaei et al. “Fourier Transform Noise Spectroscopy.” In: *npj Quantum Information* 10.1 (May 17, 2024), pp. 1–12. DOI: [10.1038/s41534-024-00841-w](https://doi.org/10.1038/s41534-024-00841-w) (cited on page 5).
- [14] Lambert Herman Koopmans. *The Spectral Analysis of Time Series*. 2nd ed. Vol. 22. Probability and Mathematical Statistics. San Diego: Academic Press, 1995 (cited on pages 5, 6, 8).
- [15] G. E. Uhlenbeck and L. S. Ornstein. “On the Theory of the Brownian Motion.” In: *Physical Review* 36.5 (Sept. 1, 1930), pp. 823–841. DOI: [10.1103/PhysRev.36.823](https://doi.org/10.1103/PhysRev.36.823) (cited on page 6).
- [16] N. G Van Kampen. “Stochastic Differential Equations.” In: *Physics Reports* 24.3 (Mar. 1, 1976), pp. 171–228. DOI: [10.1016/0370-1573\(76\)90029-6](https://doi.org/10.1016/0370-1573(76)90029-6) (cited on page 6).
- [17] N. R. Lomb. “Least-Squares Frequency Analysis of Unequally Spaced Data.” In: *Astrophysics and Space Science* 39.2 (Feb. 1, 1976), pp. 447–462. DOI: [10.1007/BF00648343](https://doi.org/10.1007/BF00648343) (cited on page 7).
- [18] J. D. Scargle. “Studies in Astronomical Time Series Analysis. II. Statistical Aspects of Spectral Analysis of Unevenly Spaced Data.” In: *The Astrophysical Journal* 263 (Dec. 1, 1982), pp. 835–853. DOI: [10.1086/160554](https://doi.org/10.1086/160554) (cited on page 7).



- [19] M. S. Bartlett. “Smoothing Periodograms from Time-Series with Continuous Spectra.” In: *Nature* 161.4096 (May 1948), pp. 686–687. DOI: [10.1038/161686a0](https://doi.org/10.1038/161686a0) (cited on page 7).
- [20] P. Welch. “The Use of Fast Fourier Transform for the Estimation of Power Spectra: A Method Based on Time Averaging over Short, Modified Periodograms.” In: *IEEE Transactions on Audio and Electroacoustics* 15.2 (June 1967), pp. 70–73. DOI: [10.1109/TAU.1967.1161901](https://doi.org/10.1109/TAU.1967.1161901) (cited on pages 7, 9).
- [21] F.J. Harris. “On the Use of Windows for Harmonic Analysis with the Discrete Fourier Transform.” In: *Proceedings of the IEEE* 66.1 (Jan. 1978), pp. 51–83. DOI: [10.1109/PROC.1978.10837](https://doi.org/10.1109/PROC.1978.10837) (cited on pages 8, 18).
- [22] Wikipedia contributors. *Window Function*. Wikipedia, The Free Encyclopedia. Mar. 20, 2025. URL: [https://en.wikipedia.org/w/index.php?title=Window\\_function&oldid=1281514999](https://en.wikipedia.org/w/index.php?title=Window_function&oldid=1281514999) (visited on 03/27/2025) (cited on page 8).
- [23] A. Nuttall. “Some Windows with Very Good Sidelobe Behavior.” In: *IEEE Transactions on Acoustics, Speech, and Signal Processing* 29.1 (Feb. 1981), pp. 84–91. DOI: [10.1109/TASSP.1981.1163506](https://doi.org/10.1109/TASSP.1981.1163506) (cited on page 8).
- [24] Ronald Forrest Fox. “Gaussian Stochastic Processes in Physics.” In: *Physics Reports* 48.3 (Dec. 1978), pp. 179–283. DOI: [10.1016/0370-1573\(78\)90145-X](https://doi.org/10.1016/0370-1573(78)90145-X) (cited on page 10).
- [25] Jan Krzywda and Łukasz Cywiński. “Adiabatic Electron Charge Transfer between Two Quantum Dots in Presence of  $1/f$  Noise.” In: *Physical Review B* 101.3 (Jan. 15, 2020), p. 035303. DOI: [10.1103/PhysRevB.101.035303](https://doi.org/10.1103/PhysRevB.101.035303). arXiv: [1909.11780](https://arxiv.org/abs/1909.11780) (cited on page 10).
- [26] Josef Schrieffer et al. “Decoherence from Ensembles of Two-Level Fluctuators.” In: *New Journal of Physics* 8 (Jan. 20, 2006), pp. 1–1. DOI: [10.1088/1367-2630/8/1/001](https://doi.org/10.1088/1367-2630/8/1/001) (cited on page 10).
- [27] Félix Beaudoin and W. A. Coish. “Microscopic Models for Charge-Noise-Induced Dephasing of Solid-State Qubits.” In: *Physical Review B* 91.16 (Apr. 29, 2015), p. 165432. DOI: [10.1103/PhysRevB.91.165432](https://doi.org/10.1103/PhysRevB.91.165432). arXiv: [1412.5536](https://arxiv.org/abs/1412.5536) (cited on page 10).
- [28] M. Mehmandoust and V. V. Dobrovitski. “Decoherence Induced by a Sparse Bath of Two-Level Fluctuators: Peculiar Features of  $1/f$  Noise in High-Quality Qubits.” In: *Physical Review Research* 6.3 (Aug. 15, 2024), p. 033175. DOI: [10.1103/PhysRevResearch.6.033175](https://doi.org/10.1103/PhysRevResearch.6.033175) (cited on page 10).
- [29] C.L. Nikias and J.M. Mendel. “Signal Processing with Higher-Order Spectra.” In: *IEEE Signal Processing Magazine* 10.3 (July 1993), pp. 10–37. DOI: [10.1109/79.221324](https://doi.org/10.1109/79.221324) (cited on page 10).
- [30] V. Chandran and S. Elgar. “A General Procedure for the Derivation of Principal Domains of Higher-Order Spectra.” In: *IEEE Transactions on Signal Processing* 42.1 (Jan. 1994), pp. 229–233. DOI: [10.1109/78.258147](https://doi.org/10.1109/78.258147) (cited on page 10).
- [31] Leigh M. Norris, Gerardo A. Paz-Silva, and Lorenza Viola. “Qubit Noise Spectroscopy for Non-Gaussian Dephasing Environments.” In: *Physical Review Letters* 116.15 (Apr. 14, 2016), p. 150503. DOI: [10.1103/PhysRevLett.116.150503](https://doi.org/10.1103/PhysRevLett.116.150503) (cited on page 10).
- [32] *welch — SciPy v1.15.2 Manual*. URL: <https://docs.scipy.org/doc/scipy-1.15.2/reference/generated/scipy.signal.welch.html> (visited on 03/31/2025) (cited on pages 11–13).
- [33] Tobias Hangleiter et al., *Qutil* version 2024.11.1, Nov. 21, 2024. Zenodo. DOI: [10.5281/ZENODO.14200303](https://doi.org/10.5281/ZENODO.14200303), (cited on page 13).
- [34] E. T. Whittaker. “XVIII.—On the Functions Which Are Represented by the Expansions of the Interpolation-Theory.” In: *Proceedings of the Royal Society of Edinburgh* 35 (Jan. 1915), pp. 181–194. DOI: [10.1017/S0370164600017806](https://doi.org/10.1017/S0370164600017806) (cited on page 15).
- [35] H. Nyquist. “Certain Topics in Telegraph Transmission Theory.” In: *Transactions of the American Institute of Electrical Engineers* 47.2 (Apr. 1928), pp. 617–644. DOI: [10.1109/T-AIEE.1928.5055024](https://doi.org/10.1109/T-AIEE.1928.5055024) (cited on page 15).
- [36] C.E. Shannon. “Communication in the Presence of Noise.” In: *Proceedings of the IRE* 37.1 (Jan. 1949), pp. 10–21. DOI: [10.1109/JRPROC.1949.232969](https://doi.org/10.1109/JRPROC.1949.232969) (cited on page 15).
- [37] David M. Pozar. *Microwave Engineering*. Fourth edition. Hoboken, NJ: John Wiley & Sons, Inc, 2012. 1 p. (cited on page 16).
- [38] Till Huckemann. PhD thesis. Aachen: RWTH Aachen University, 2025 (cited on page 21).

- [39] Dorit Aharonov, Alexei Kitaev, and John Preskill. “Fault-Tolerant Quantum Computation with Long-Range Correlated Noise.” In: *Physical Review Letters* 96.5 (Feb. 7, 2006), p. 050504. doi: [10.1103/PhysRevLett.96.050504](https://doi.org/10.1103/PhysRevLett.96.050504) (cited on page 22).
- [40] Naomi H. Nickerson and Benjamin J. Brown. “Analysing Correlated Noise on the Surface Code Using Adaptive Decoding Algorithms.” In: *Quantum* 3 (Apr. 8, 2019), p. 131. doi: [10.22331/q-2019-04-08-131](https://doi.org/10.22331/q-2019-04-08-131). arXiv: [1712.00502](https://arxiv.org/abs/1712.00502) (cited on page 22).
- [41] B. D. Clader et al. “Impact of Correlations and Heavy Tails on Quantum Error Correction.” In: *Physical Review A* 103.5 (May 24, 2021), p. 052428. doi: [10.1103/PhysRevA.103.052428](https://doi.org/10.1103/PhysRevA.103.052428) (cited on page 22).
- [42] *csd — SciPy v1.15.2 Manual*. URL: <https://docs.scipy.org/doc/scipy-1.15.2/reference/generated/scipy.signal.csd.html> (visited on 04/15/2025) (cited on page 23).
- [43] J.S. Rojas-Arias et al. “Spatial Noise Correlations beyond Nearest Neighbors in  $^{28}\text{Si}/\text{Si-Ge}$  Spin Qubits.” In: *Physical Review Applied* 20.5 (Nov. 9, 2023), p. 054024. doi: [10.1103/PhysRevApplied.20.054024](https://doi.org/10.1103/PhysRevApplied.20.054024) (cited on page 23).
- [44] J. Yoneda et al. “Noise-Correlation Spectrum for a Pair of Spin Qubits in Silicon.” In: *Nature Physics* (Oct. 9, 2023). doi: [10.1038/s41567-023-02238-6](https://doi.org/10.1038/s41567-023-02238-6) (cited on page 23).
- [45] Pascal Cerfontaine et al. “Closed-Loop Control of a GaAs-based Singlet-Triplet Spin Qubit with 99.5% Gate Fidelity and Low Leakage.” In: *Nature Communications* 11.1 (Dec. 2020), p. 4144. doi: [10.1038/s41467-020-17865-3](https://doi.org/10.1038/s41467-020-17865-3) (cited on pages 76, 87, 88).
- [46] Łukasz Cywiński et al. “How to Enhance Dephasing Time in Superconducting Qubits.” In: *Physical Review B* 77.17 (May 13, 2008), p. 174509. doi: [10.1103/PhysRevB.77.174509](https://doi.org/10.1103/PhysRevB.77.174509) (cited on page 79).
- [47] Todd J. Green et al. “Arbitrary Quantum Control of Qubits in the Presence of Universal Noise.” In: *New Journal of Physics* 15.9 (Sept. 12, 2013), p. 095004. doi: [10.1088/1367-2630/15/9/095004](https://doi.org/10.1088/1367-2630/15/9/095004). arXiv: [1211.1163](https://arxiv.org/abs/1211.1163) (cited on pages 79, 81).
- [48] P C Moan, J A Oteo, and J Ros. “On the Existence of the Exponential Solution of Linear Differential Systems.” In: *Journal of Physics A: Mathematical and General* 32.27 (1999), pp. 5133–5139. doi: [10.1088/0305-4470/32/27/311](https://doi.org/10.1088/0305-4470/32/27/311) (cited on page 79).
- [49] Tobias Hangleiter, *Lindblad\_mc\_tools* Aug. 8, 2025. URL: [https://git.rwth-aachen.de/tobias.hangleiter/lindblad\\_mc\\_tools](https://git.rwth-aachen.de/tobias.hangleiter/lindblad_mc_tools) (cited on page 85).
- [50] G. Lindblad. “On the Generators of Quantum Dynamical Semigroups.” In: *Communications in Mathematical Physics* 48.2 (June 1976), pp. 119–130. doi: [10.1007/BF01608499](https://doi.org/10.1007/BF01608499) (cited on page 85).
- [51] Vittorio Gorini, Andrzej Kossakowski, and E. C. G. Sudarshan. “Completely Positive Dynamical Semigroups of N-level Systems.” In: *Journal of Mathematical Physics* 17.5 (1976), p. 821. doi: [10.1063/1.522979](https://doi.org/10.1063/1.522979) (cited on page 85).
- [52] Christopher J. Wood and Jay M. Gambetta. “Quantification and Characterization of Leakage Errors.” In: *Physical Review A* 97.3 (Mar. 8, 2018), p. 032306. doi: [10.1103/PhysRevA.97.032306](https://doi.org/10.1103/PhysRevA.97.032306) (cited on page 87).
- [53] J. R. Johansson, P. D. Nation, and Franco Nori. “QuTiP: An Open-Source Python Framework for the Dynamics of Open Quantum Systems.” In: *Computer Physics Communications* 183.8 (Aug. 1, 2012), pp. 1760–1772. doi: [10.1016/j.cpc.2012.02.021](https://doi.org/10.1016/j.cpc.2012.02.021) (cited on page 89).



# Glossary

## A

**API** application programming interface. 16

**ASD** amplitude spectral density. 16, 86

## C

**CPTP** completely-positive trace preserving. 86

**CS** computational subspace. 87, 88

**CSD** cross power spectral density. 22, 23

## D

**DAQ** data acquisition. 3, 9–13, 15, 16, 21

**DCG** dynamically corrected gate. 88

**DD** dynamical decoupling. 4

**DUT** device under test. 4

## E

**ENBW** equivalent noise bandwidth. 18

## F

**FF** filter function. 76, 89, 90

**FFT** fast Fourier transform. 10

## G

**GGM** generalized Gell-Mann. 87

**GKSL** Gorini-Kossakowski-Sudarshan-Lindblad. ix, 76, 85, 89, 90

**GRAPE** gradient ascent pulse engineering. ix, 88, 89

**GUI** graphical user interface. 19

## I

**IQ** in-phase/quadrature. 88

## L

**LIA** lock-in amplifier. 4, 10, 15

## M

**MC** Monte Carlo. 85, 86, 89, 90

**ME** Magnus expansion. 76, 79–81

## P

**PSD** power spectral density. viii, 3, 5–7, 9–11, 13, 15–18, 21–23, 86, 89

## Q

**QFT** quantum Fourier transform. ix, 76, 87–90

## R

**RMS** root mean square. 4, 6, 16–18

## T

**TIA** transimpedance amplifier. 13

**TLF** two-level fluctuator. 10

# Figure source files and parameters

2.1	Generated by img/tikz/spectrometer/lockin_dut.tex. . . . .	4
2.2	Generated by img/py/spectrometer/lorentz.py. . . . .	6
2.3	Generated by img/py/spectrometer/pyspeck.py. . . . .	8
2.4	Generated by img/py/spectrometer/pyspeck.py. . . . .	8
2.5	Generated by img/py/spectrometer/pyspeck.py. . . . .	9
2.6	Generated by img/tikz/spectrometer/daq_settings.tex. . . . .	10
3.1	Generated by img/tikz/spectrometer/speck_tree.tex. . . . .	11
3.2	Generated by img/py/spectrometer/pyspeck_workflow.py. . . . .	16
3.3	Generated by img/py/spectrometer/pyspeck_workflow.py. . . . .	17
3.4	Generated by img/py/spectrometer/pyspeck_workflow.py. . . . .	17
3.5	Generated by img/py/spectrometer/pyspeck_workflow.py. . . . .	17
3.6	Generated by img/py/spectrometer/pyspeck_workflow.py. . . . .	18
3.7	Generated by img/py/spectrometer/pyspeck_workflow.py. . . . .	18
3.8	Generated by img/py/spectrometer/pyspeck_live_view.py. . . . .	20
6.1	Illustration of gate sequence . . . . .	39
6.2	Generated by img/py/filter_functions/benchmark_monte_carlo.py. . . . .	51
7.1	Generated by img/py/filter_functions/monte_carlo_filter_functions.py. . . . .	54
7.2	Generated by img/py/filter_functions/monte_carlo_filter_functions.py. . . . .	55
7.3	Generated by img/py/filter_functions/monte_carlo_filter_functions.py. . . . .	56
9.1	Generated by img/py/filter_functions/cnot_FF.py. . . . .	63
9.2	Generated by img/py/filter_functions/periodic_driving.py. . . . .	66
9.3	Generated by img/py/filter_functions/randomized_benchmarking.py. . . . .	69
9.4	Generated by img/tikz/circuits/qft.tex. Generated by img/py/filter_functions/quantum_fourier_transform.py. . . . .	71
9.5	Generated by img/py/filter_functions/quantum_fourier_transform.py. . . . .	72
A.1	Generated by img/py/filter_functions/cnot_FF.py. . . . .	88
A.2	Generated by img/py/filter_functions/quantum_fourier_transform.py. . . . .	89
A.3	Generated by img/py/filter_functions/quantum_fourier_transform.py. . . . .	90

# Declaration of Authorship

I, Tobias Hangleiter, declare that this thesis and the work presented in it are my own and has been generated by me as the result of my own original research.

I do solemnly swear that:

1. This work was done wholly or mainly while in candidature for the doctoral degree at this faculty and university;
2. Where any part of this thesis has previously been submitted for a degree or any other qualification at this university or any other institution, this has been clearly stated;
3. Where I have consulted the published work of others or myself, this is always clearly attributed;
4. Where I have quoted from the work of others or myself, the source is always given. This thesis is entirely my own work, with the exception of such quotations;
5. I have acknowledged all major sources of assistance;
6. Where the thesis is based on work done by myself jointly with others, I have made clear exactly what was done by others and what I have contributed myself;
7. Parts of this work have been published before as:

- [1] Pascal Cerfontaine, Tobias Hangleiter, and Hendrik Bluhm. “Filter Functions for Quantum Processes under Correlated Noise.” In: *Physical Review Letters* 127.17 (Oct. 18, 2021), p. 170403. doi: [10.1103/PhysRevLett.127.170403](https://doi.org/10.1103/PhysRevLett.127.170403).
- [2] Thomas Descamps, Feng Liu, Tobias Hangleiter, Sebastian Kindel, Beata E. Kardynał, and Hendrik Bluhm. “Millikelvin Confocal Microscope with Free-Space Access and High-Frequency Electrical Control.” In: *Review of Scientific Instruments* 95.8 (Aug. 9, 2024), p. 083706. doi: [10.1063/5.0200889](https://doi.org/10.1063/5.0200889).
- [3] Tobias Hangleiter, Pascal Cerfontaine, and Hendrik Bluhm. “Filter-Function Formalism and Software Package to Compute Quantum Processes of Gate Sequences for Classical Non-Markovian Noise.” In: *Physical Review Research* 3.4 (Oct. 18, 2021), p. 043047. doi: [10.1103/PhysRevResearch.3.043047](https://doi.org/10.1103/PhysRevResearch.3.043047).

---

Aachen, September 7, 2025.